Energy & Buildings 373 (2026) 118398

Contents lists available at ScienceDirect

Energy & Buildings

journal homepage: www.elsevier.com/locate/enbuild

Evaluating the performance of seasonal borehole thermal storage in 5th generation district heating and cooling networks

Hector Bastida [a,*], Meysam Qadrdan [a], Wu Gao [b,c,d,e]

[a] School of Engineering, Cardiff University, Queen's Buildings, The Parade, Cardiff, CF24 3AA, Wales, UK
[b] Institute of Geotechnical Engineering, Zhejiang University, Hangzhou, 310058, China
[c] Institute of Hypergravity Science and Technology, Zhejiang University, Hangzhou, 310058, China
[d] MOE Key Laboratory of Soft Soils and Geoenvironmental Engineering, Zhejiang University, Hangzhou, 310058, China
[e] State Key Laboratory of Soil Pollution Control and Safety, Zhejiang University, Hangzhou, 310058, China

ARTICLE INFO

Keywords:
Borehole field
Water-to-water heat pump
Low-temperature thermal network
Seasonal coefficient of performance (SCOP)

ABSTRACT

The operating temperature range of borehole fields includes low-temperature levels that may be suitable for fifth-generation district heating and cooling (5GDHC) networks, while also enabling bidirectional heat exchange and seasonal thermal storage. However, their performance depends on network temperature management, the balance between annual heat extraction and injection, and local ground conditions. This study investigates how supply- and return-temperature set-points affect short-term heat-pump coefficient of performance (COP) through their influence on the borehole entering-fluid temperature; whether cooling-season charging improves winter COP and seasonal coefficient of performance (SCOP) while mitigating long-term thermal drift; and whether year-round bidirectional operation or explicit summer recharge better supports multi-year thermal stability. An integrated TRNSYS model combining a low-temperature network, building-level water-to-water heat pumps, and a composite borehole-field model was used to simulate hourly and multi-year operation under three ground configurations, including an idealised representation of groundwater-induced temperature stabilisation. The results show that the heat pumps meet building thermal demands within the 5GDHC operating range, achieving SCOP values between 3.41 and 3.88. Maintaining a higher borehole entering-fluid temperature through appropriate temperature and mass-flow control improves heat-pump COP. Cooling-season charging improves winter performance and mitigates thermal drift when sufficient injected heat is retained in the ground. Balanced thermal-demand operation therefore provides greater multi-year thermal stability than heating-dominated operation with limited recharge.

1. Introduction

The building sector remains one of the largest energy end-use sectors worldwide. The United Nations Environment Programme (UNEP) [1] reported that the buildings and construction sector accounts for approximately 32% of global energy consumption and 34% of global (CO_2) emissions. Similarly, the International Energy Agency (IEA) [2] estimated that buildings account for around 30% of global energy demand, with space and water heating representing a major share of residential energy consumption. Consequently, the decarbonisation of heating constitutes a key element of the transition towards net-zero energy systems. Sadeghi et al. [3] analysed heat-pump deployment and performance in Norway, showing that ground-source heat pumps can provide higher performance than air-source systems under cold climatic conditions, although at a higher initial cost. At the district scale, Li et al. [4] demonstrated that integrating fifth-generation district heating and cooling (5GDHC) with seasonal borehole thermal energy storage (BTES) can improve thermal balancing while reducing peak electricity demand and greenhouse-gas emissions. These characteristics make the coordination of thermal loads increasingly important for enabling load shifting and operational flexibility beyond the individual-building level.

District heating and cooling (DHC) networks can support heat decarbonisation by integrating diverse thermal resources and coordinating energy supply across connected users. Kontu et al. [5] demonstrated that incorporating large-scale heat pumps into existing district heating systems can reduce fossil-fuel use and diversify heat production, with particularly strong potential in smaller networks. Within this context, 5GDHC networks have emerged as a near-ambient-temperature architecture. Yao et al. [6] identified distributed end-user heat pumps, near-ambient network temperatures, and the provision of both heating and

* Corresponding author.
E-mail addresses: BastidaHernandezJ@cardiff.ac.uk (H. Bastida), QadrdanM@cardiff.ac.uk (M. Qadrdan), gaowu@zju.edu.cn (W. Gao).

https://doi.org/10.1016/j.enbuild.2026.118398
Received 20 May 2026; Received in revised form 8 October 2026; Accepted 13 October 2026
Available online 16 October 2026
0378-7788/© 2026 The Author(s). Published by Elsevier B.V. This is an open access article under the CC BY license (http://creativecommons.org/licenses/by/4.0/).

Nomenclature

Abbreviations

5GDHC	Fifth-generation district heating and cooling
BHE	Borehole heat exchanger
BTES	Borehole thermal energy storage
COP	Coefficient of performance
DHC	District heating and cooling
FLS	Finite line-source
SCOP	Seasonal coefficient of performance
TRNSYS	Transient system simulation environment

Greek symbols

α	Thermal diffusivity [m^2/s]
Δ	Difference or increment in the associated variable
ϵ	Heat-exchanger effectiveness [–]
η	Efficiency [–]
λ	Thermal conductivity [W/(m K)]
μ	Dynamic viscosity [Pa s]
ρ	Density [kg/m^3]

Variables

A	Area [m^2]
c	Heat-capacity rate [W/°C]
c_p	Specific heat capacity [J/(kg°C)]
D	Pipe diameter [m]
f_D	Darcy friction factor [-]
H	Borehole depth [m]
L	Pipe length [m]
m	Mass [kg]
$\dot{m}$	Mass flow rate [kg/s]
NTU	Number of transfer units [-]
p	Pressure [Pa]
P	Electrical power [W]
Q	Heat-transfer rate [W]
r	Pipe radius [m]
R	Thermal resistance [°C/W]
s	Borehole spacing [m]
T	Temperature [°C]
t	Time [s]
U	Heat-transfer coefficient [$W/(m^2°C)$]

Subscripts

abs	Absorbed
amb	Ambient
bh	Borehole field
bt	Buffer tank
c	Cold stream
f	Fluid
g	Ground or grout, depending on context
gr	Grout
h	Hot stream
HE	Heat-exchanger interface
hp	Heat pump
hx	Heat exchanger
i	Inlet
in	Entering
L	Load side or ground layer
m	Main hydraulic pump
o	Outlet
out	Leaving
p	Primary hydraulic pump
rej	Rejected
ret	Return
s	Secondary hydraulic pump
S	Source side
sup	Supply

Superscripts

bt	Buffer tank
hp	Heat pump
hx	Heat exchanger

cooling as distinctive characteristics of these systems. Gjoka et al. [7] further highlighted that bidirectional energy flows can exploit heating and cooling demand synergies between users, while identifying limited design guidelines and implementation barriers as continuing challenges to wider deployment. Consequently, a key research challenge is to identify which low-grade thermal resources can most effectively support near-ambient network operation while maintaining efficient and stable system performance.

Among the candidate resources, shallow geothermal energy is particularly attractive for 5GDHC networks because it provides access to locally available low-temperature heat sources and sinks. Buffa et al. [8], in their review of 40 operating 5GDHC networks in Europe, identified geothermal resources among the low-temperature sources that can be effectively exploited by near-ambient thermal networks. Boesten et al. [9] showed through the Mijnwater system that shallow geothermal resources, combined with bidirectional energy exchange and thermal storage, can contribute to balancing renewable heating and cooling supply at the urban scale. More recently, Gjoka et al. [10] evaluated a ground-based 5GDHC configuration using borehole heat exchangers (BHEs), highlighting geothermal energy as one of the potential source–sink options for 5GDHC operation under mild climatic conditions. Evidence from existing systems also supports this integration: the survey of 53 German 5GDHC networks conducted by Wirtz et al. [11] identified geothermal probes and horizontal geothermal collectors as the most frequently adopted thermal sources.

Beyond their role as an immediate heat source or sink, geothermal systems can also provide seasonal thermal storage. Zeh et al. [12] demonstrated that large-scale shallow geothermal collector systems can shift heating and cooling loads seasonally by storing surplus thermal energy in the ground. Similarly, Figueira et al. [13] reviewed practical shallow-geothermal DHC case studies and highlighted their potential to support low-temperature heating and cooling networks through efficient use of the subsurface as both a thermal source and sink. For borehole-based storage specifically, Sadeghi et al. [14] showed that integrating borehole thermal energy storage (BTES) into DHC systems can improve system efficiency, while emphasising that its performance depends strongly on thermal design and subsurface conditions. Consequently, although borehole fields can operate as a heat source during winter and a heat sink during summer, their short-term operation also influences the longer-term thermal evolution of the surrounding ground. These ground thermal conditions, in turn, determine the temperatures available to the decentralised heat pumps and therefore influence both instantaneous and seasonal system performance.

The performance of borehole fields must therefore be understood across two coupled time horizons: short-term operation, in which hourly to daily load variations influence entering-fluid temperature and heat-pump coefficient of performance (COP), and long-term operation, in which seasonal recharge and cumulative thermal imbalance determine the evolution of ground conditions. Lanahan and Tabares-Velasco [15] reviewed BTES modelling and system design, emphasis-

ing the importance of seasonal storage behaviour and its integration with the wider thermal system. Long-term operational evidence is provided by Sibbitt et al. [16], who demonstrated through five years of monitoring at the Drake Landing Solar Community that summer heat stored in a borehole field can be effectively recovered during subsequent heating seasons. Mesquita et al. [17] extended this assessment to ten years of operation, confirming the reliable long-term performance of seasonal borehole thermal storage. More broadly, Dang et al. [18] identified thermal balancing and operational control among the key considerations for effective 5GDHC operation. More recently, Zhi et al. [19] investigated a large-scale ground-source heat-pump system after nine years of operation and examined the influence of building-load characteristics and thermal imbalance on its long-term performance. These findings indicate that borehole performance cannot be assessed solely through annual energy balances or peak design conditions; rather, both instantaneous entering-fluid temperatures and cumulative thermal balance must remain within acceptable limits over time.

This requirement has important implications for borehole sizing and design. Borehole depth, spacing, and field layout must satisfy peak extraction and rejection demands while maintaining acceptable temperature limits. Kavanaugh and Rafferty [20] presented established design procedures and best practices for ground-source heat-pump systems, including the sizing and configuration of ground heat exchangers. Ahmadfard and Bernier [21] proposed a multi-level approach for sizing vertical ground heat exchangers, allowing different calculation methods to be selected according to the information available to the designer. For seasonal storage applications, Gao et al. [22] highlighted that BTES performance depends on borehole arrangement, ground properties, and operating parameters, as well as on the coordination of charging and discharging with the wider thermal system. More recently, Miceli et al. [23] introduced a g-function-based BTES model with a novel load-aggregation scheme that improves computational accuracy during rapid transitions between charging and discharging and provides a basis for future digital-twin applications. Nevertheless, sizing alone is not sufficient; operational strategies and temperature control must also be considered when analysing short- and long-term borehole performance in practice.

To address these issues, modelling approaches must represent both the transient thermal response of the ground and the internal heat-transfer processes within the borehole. Lamarche and Beauchamp [24] developed an analytical finite line-source (FLS) formulation for predicting the transient thermal response of geothermal boreholes. Building on this approach, Cimmino and Bernier [25] proposed a semi-analytical method for generating g-functions that accounts for variations in heat extraction along and between boreholes, while Cimmino [26] subsequently introduced similarity-based techniques to reduce the computational cost of g-function calculations for large and irregular borehole fields. To represent more realistic geological conditions, Erol and François [27] extended the FLS framework to multilayer ground while accounting for groundwater-induced advection and dispersion, whereas Hu [28] developed a multilayer analytical model incorporating groundwater flow to evaluate long-term borehole temperature response under unbalanced seasonal loads. More recently, Gao and Qadrdan [29] developed a composite analytical model for stratified ground that accounts for ground heterogeneity, borehole thermal interactions, and variations in heat flux along the borehole depth.

At the district scale, recent studies have integrated BTES models with wider thermal-network analyses. Chaudhry et al. [30] proposed a robust-design framework for 5GDHC networks, while Romanov et al. [31] assessed data-centre waste-heat recovery with shallow BTES under different network temperature levels. Li et al. [32] showed that seasonal BTES can mitigate the temporal mismatch between heating and cooling demands in 5GDHC networks, whereas Fiorentini et al. [33] examined how BTES size and operating temperature affect storage and connected heat-pump performance. More detailed approaches have also been developed: Pour Ahmadiyan and Nord [34] employed a hybrid g-function model, and Yang et al. [35] incorporated g-functions into a multi-year optimisation framework. However, these approaches generally represent the subsurface through effective ground properties and do not explicitly resolve stratification, groundwater flow, or the contribution of individual ground layers. This gap motivates layer-resolved analyses that capture both short- and long-term borehole behaviour within district-scale simulations. However, the benefits of improved borehole conditions are ultimately realised through the heat pump, which converts near-ambient loop temperatures into useful heating or cooling. It is therefore necessary to integrate borehole thermal behaviour with heat-pump dynamics within a simulation framework that captures operating conditions and seasonal efficiency metrics.

In 5GDHC systems, decentralised water–to–water heat pumps play a central role in determining both instantaneous and seasonal performance. Their COP depends strongly on the source-side temperature, load-side set-points, and mass-flow control. The use of water–to–water heat pumps with boreholes as the energy source follows the same thermodynamic principles. Return-temperature management is particularly influential: lower load-side return temperatures generally improve the heating COP and reduce the immediate thermal stress on the borehole field, but they may also accelerate ground-temperature depletion during winter operation. Conversely, higher return temperatures during cooling can enhance thermal charging of the ground. This creates a fundamental trade-off. The same control variables that improve short-term heat-pump performance may also alter the long-term charging and discharging trajectory of the ground, thereby affecting future operating conditions. Chaudhry et al. [30] showed through a robust-design framework that feasible and optimal 5GDHC operating temperatures are sensitive to uncertain energy-market conditions and tariffs. At the operational level, Droste and Schwartz [36] demonstrated the emerging potential of data-driven and machine-learning-assisted model predictive control (MPC) for 5GDHC operation, although such approaches typically focus on relatively short time horizons and do not explicitly capture long-term ground thermal drift. Consequently, there remains a need for studies that examine how temperature management influences both heat-pump performance and borehole thermal evolution.

Despite the growing literature on 5GDHC systems and borehole integration, the detailed influence of supply- and return-temperature management on (i) short-term heat-pump performance, (ii) seasonal storage effectiveness, and (iii) multi-year thermal drift in layered ground conditions remains insufficiently quantified. Yao et al. [6] identified network temperature, distributed heat pumps, and operational control as key features of 5GDHC systems, while also highlighting continuing technical and operational research gaps. Chaudhry et al. [30] investigated feasible 5GDHC network temperatures within a robust-design framework, although the effect of load-side return-temperature control on borehole thermal conditions was not explicitly isolated. For seasonal storage, Miceli et al. [23] demonstrated that BTES performance is sensitive to the temporal distribution of charging and discharging loads, particularly during transitions between operating modes. These findings indicate that the operating strategy determines not only the amount of heat extracted from and injected into the ground, but also its long-term thermal evolution. Addressing this gap therefore requires an integrated analysis linking network temperature management, heat-pump COP/SCOP, seasonal borehole charging, and multi-year ground thermal behaviour under stratified ground conditions.

Accordingly, this study addresses the following research questions:

- How do the supply and return temperature set-points, through the coupled interaction between the heat pumps and borehole field, influence short-term heat-pump COP and borehole entering-fluid temperature?

- To what extent can cooling-season charging improve subsequent winter COP and SCOP and mitigate long-term thermal drift, and how does this depend on return-temperature management?
- Which operating strategy better supports seasonal performance and multi-year thermal stability: using the borehole field as a bidirectional source/sink throughout the year or operating it primarily as a seasonal store with explicit summer recharge?

To answer these questions, this paper develops an integrated 5GDHC model in TRNSYS that combines an ambient distribution loop with a composite borehole-field model. Different ground-layer configurations were examined, including cases with groundwater flow, under three operating scenarios: a heating-dominated mode, a no-recharge case in which cooling-season borehole use was suppressed, and a balanced thermal-load case in which cooling demand equals heating demand. Performance was assessed using short-term COP, SCOP, and long-term indicators of borehole thermal behaviour, including thermal drift. By linking load-side temperature set-points and mass-flow control to both short-term efficiency and multi-year thermal stability, the study provides a detailed explanation of how heat-pump operating conditions influence borehole-field performance.

The remainder of the paper is structured as follows. Section 2 presents the integrated modelling framework and the main component models. Section 3 describes the case study, load profiles, and operating scenarios. Section 4 reports and discusses the results in terms of short-term heat-pump performance, seasonal behaviour, and long-term borehole thermal response. Section 5 discusses the broader implications of the main findings, together with the limitations of the study. Finally, Section 6 summarises the main findings and outlines the implications for system design and future research.

2. System description

This section outlines the integrated simulation framework used to represent the interaction among the borehole field, the fifth-generation district heating and cooling (5GDHC) system, and the time-varying thermal demands of the connected buildings (Fig. 1). The borehole field is connected directly to the two-pipe ambient network loop, without a central heat pump, because both operate under compatible low-temperature conditions. Thus, the fluid leaving the borehole field can be supplied directly to the ambient-temperature network without requiring its temperature to be boosted by a central heat pump. This configuration differs from conventional or warm district-heating architectures in which a central heat pump raises the network supply temperature. In cold or near-ambient bidirectional networks, including configurations commonly associated with 5GDHC, temperature upgrading can instead be performed locally by decentralised heat pumps at the building substations [37,38]. The network considered here therefore does not seek to maintain a conventional high supply temperature at the central source; rather, the borehole field supplies the low-temperature loop, while the building-level water-to-water heat pumps provide the required temperature lift to satisfy the local heating demand. During the heating season, the borehole outlet feeds the warm pipe, from which the buildings extract heat, while the cool pipe returns water to the borehole inlet. During the cooling season, these connections are reversed: the borehole outlet feeds the cool pipe, while the warm pipe transports heat rejected by the buildings to the borehole inlet for seasonal ground recharge. To avoid confusion when presenting and comparing the simulation results, the labels of the borehole-field inlet ($T_{\mathrm{bh},i}$) and outlet ($T_{\mathrm{bh},o}$) are defined according to the heating-season configuration and retained consistently throughout the manuscript, including when the network circulation changes during cooling operation, as shown in Fig. 1.

Each building is connected to the network through a decentralised substation comprising circulation pumps to regulate the flow rate, a heat exchanger, a reversible water-to-water heat pump, a storage tank, and control valves that switch the flow direction when the operating mode changes between heating and cooling. The local heat pumps upgrade the network temperature for space heating and transfer heat from the buildings to the network during cooling operation, as detailed in Section 2.2. The 5GDHC component models and basic configuration were previously presented in [39], while the borehole model was presented and validated in [29]. Therefore, only the principal assumptions, governing interactions, and key equations required to understand the present study are summarised here.

The framework was designed to capture both short-term and seasonal behaviour. At short time scales, the model resolves how loop temperature, flow rate, and heat-pump operating conditions affect instantaneous heating and cooling delivery and COP. At longer time scales, it tracks the cumulative thermal effects of winter heat extraction and summer heat injection on borehole temperature evolution, thermal recovery, and long-term system balance [7,40]. This multi-time-scale representation is essential for 5GDHC systems because the network, heat pumps, and borehole field do not operate independently. The borehole field determines the source-side temperature available to the network, while network operation and building demands determine the thermal load imposed on the ground.

2.1. Borehole model

Heat transfer around each vertical BHE is represented by coupling an internal borehole model with an external ground-response model. The external domain is described using a finite line-source (FLS) formulation, which captures the transient thermal response of the ground with sufficient accuracy for long-term simulations while remaining computationally efficient [24]. Groundwater advection can, in principle, be represented using extensions such as the moving finite-line-source model. However, groundwater advection was not explicitly solved in the present simulations. Instead, the groundwater-influenced scenarios were represented using the idealised temperature-stabilisation condition described in Section 3.1. This is particularly important in the present work, where annual and multi-year behaviour must be analysed across several operating scenarios. Details of the multilayer composite formulation adopted here are reported in [29]. The internal borehole is represented by a resistance–capacitance network that resolves the fluid temperatures in the downward and upward legs of the U-tube, the grout thermal mass, and heat exchange with the borehole wall [41,42]. Fig. 2 illustrates the borehole geometry, the U-tube configuration, the surrounding soil layers, and the principal geometric and thermal parameters used in the model. A representative nodal energy balance for the downward leg is written as follows:

$$m_f c_{p,f} \frac{dT_{f1,n}}{dt} = \dot{m}_f c_{p,f} \left(T_{f1,n-1} - T_{f1,n}\right) + \frac{T_{f2,n} - T_{f1,n}}{R_{ff}} + \frac{T_{g,n} - T_{f1,n}}{R_{fg}}. \quad (1)$$

where m_f (kg) is the fluid mass, $c_{p,f}$ (J/(kg°C)) is the fluid specific heat, and $\dot{m}_f$ (kg/s) is the fluid mass flow rate. The variables $T_{f1,n}$, $T_{f2,n}$, and $T_{g,n}$ (°C) denote the fluid temperatures in the downward and upward legs and the grout temperature at axial node n, respectively. The equivalent thermal resistance between the two legs of the borehole is denoted by R_{ff}, while the resistance between the fluid and grout is denoted by R_{fg} (m°C/W). The borehole-wall temperature is supplied by the external FLS solution, thereby linking the short-term internal borehole dynamics with the long-term ground response.

This coupling allows the model to represent two key thermal behaviours. First, over minutes to hours, the borehole outlet temperature depends on the fluid flow rate, thermal resistances, and the thermal capacities of the fluid and grout. These variables directly affect the heat-pump source temperature and, consequently, the instantaneous COP. Second, over weeks to months, the accumulated thermal response

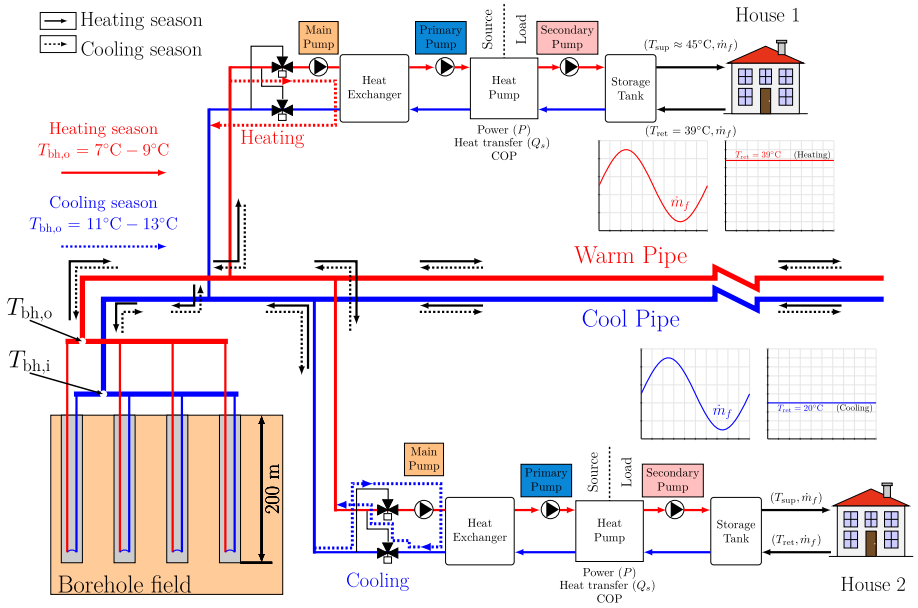


Fig. 1. Integrated schematic of borehole field, 5GDHC system, decentralised water-to-water heat pumps, and thermal loads.

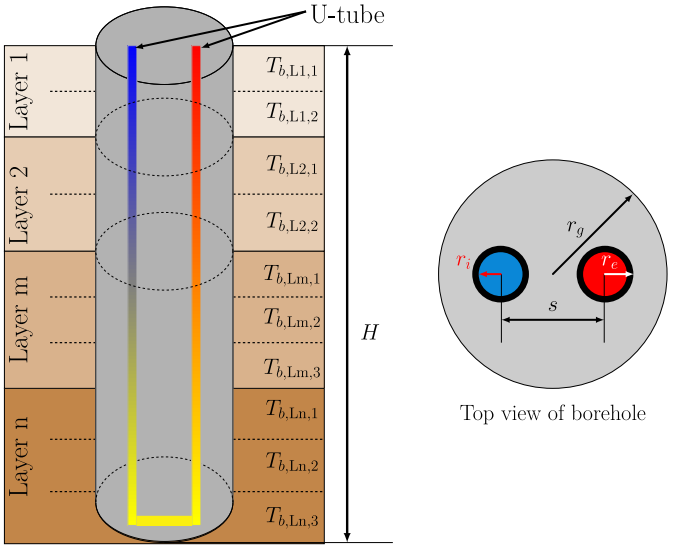


Fig. 2. Schematic of a single vertical borehole heat exchanger and associated geometric and thermal parameters.

of the surrounding ground determines seasonal charging and discharging, thermal recovery, and potential temperature drift under imbalanced annual loads [16,43].

The borehole field is parametrised by borehole depth H (m), spacing s (m), radius r (m), U-tube dimensions, grout properties, and field layout. In addition, the ground is modelled as vertically stratified, allowing each soil layer to be assigned distinct values of thermal conductivity, density, and specific heat capacity. This is important because both ground stratification and borehole spacing influence thermal interference between neighbouring boreholes and, consequently, the long-term temperature available to the network.

2.2. 5GDHC system and building interface

The 5GDHC system was modelled as an ambient-temperature bidirectional loop that connects the buildings and the borehole field through warm and cool pipes, as shown in Fig. 1. In contrast to conventional high-temperature district heating, the loop operates close to ambient temperature, typically within the range of 5–25 °C. This reduces distribution losses and facilitates heat sharing between users, although higher flow rates may be required to deliver the same thermal capacity [8,9].

At each network node, mass conservation is imposed as

$$\sum \dot{m}_{\text{in}} - \sum \dot{m}_{\text{out}} = 0, \tag{2}$$

where $\dot{m}_{\text{in}}$ and $\dot{m}_{\text{out}}$ (kg/s) denote the mass flow rates entering and leaving the node, respectively. The pressure drop along each pipe segment is evaluated using the Darcy–Weisbach relation:

$$p_{\text{in}} - p_{\text{out}} = \frac{8 L f_D \dot{m}_f^2}{1000 \rho \pi^2 D^5}, \tag{3}$$

where p_{in} and p_{out} (Pa) are the inlet and outlet pressures, L and D (m) are the pipe length and diameter, ρ (kg/m^3) is the fluid density, and f_D is the Darcy friction factor. Pipe heat exchange with the surrounding soil is represented using lumped energy balances based on an equivalent thermal resistance that accounts for internal convection, pipe-wall conduction, insulation, and external ground resistance. This level of detail is sufficient for network-scale studies, where the main interest lies in the interaction between temperature set-points, mass-flow control, and heat-pump performance, rather than detailed hydraulic dynamics.

Because the network is bidirectional, the flow direction may change in individual branches depending on local demand and source conditions. Consequently, the hydraulic and thermal calculations are solved iteratively until network-wide mass and energy balances are satisfied under the imposed operating set-points, following the methodology described in [39].

Each building was connected to the network through a local energy-transfer interface comprising a heat exchanger, a water-to-water heat pump, circulation pumps, and a water tank. A set of control valves located between the network loop and the heat exchanger switches the hydraulic connections according to the operating mode. During heating, the heat exchanger is supplied from the warm pipe and returns water to the cool pipe; during cooling, it is supplied from the cool pipe and returns water to the warm pipe. This arrangement maintains the same direction of circulation through the heat exchanger in both operating modes, as shown in Fig. 1. The controller regulates heat-pump operation and mass flow rate to satisfy the tank supply-temperature set-point. Detailed building thermal dynamics are outside the scope of this

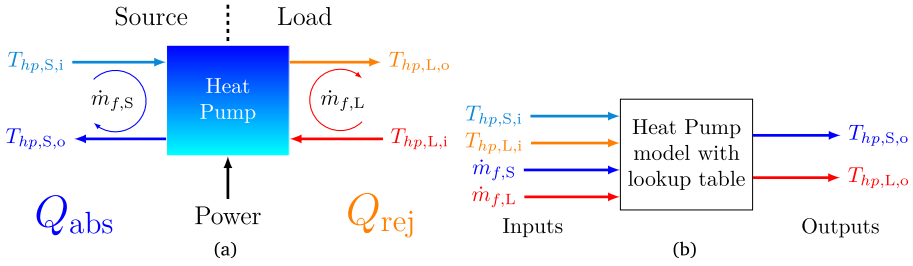


Fig. 3. Water-to-water heat pump model: (a) schematic of the heat pump unit and (b) model inputs and outputs.

paper. Instead, the building load was imposed through a time-varying tank-side mass flow rate, while fixed return temperatures were assumed for heating and cooling operation. The fixed return temperatures and the corresponding time-varying mass-flow-rate profiles are illustrated by the small plots included in the schematic of Fig. 1 to clarify how these boundary conditions are imposed at the building interface. These assumptions and their implementation are described in further detail in the following section.

2.3. Heat pump

Water-to-water heat pumps provide the temperature lift or drop between the thermal network and the building heating or cooling circuit. Their performance is strongly influenced by the inlet temperatures and mass flow rates on both the source and load sides. For this reason, the heat pump is represented using performance maps that relate the source-side inlet temperature $T_{hp,S,i}$, load-side inlet temperature $T_{hp,L,i}$, and corresponding mass flow rates to thermal capacity and electrical power [39]. This lookup-table approach captures the non-linear behaviour of the vapour-compression cycle at low computational cost, making it suitable for annual simulations.

The heat absorbed at the evaporator, Q_{abs} (W), is evaluated from the map outputs as

$$Q_{abs} = Q_{rej} - P_{hp}, \tag{4}$$

where Q_{rej} is the heat rejected at the condenser and P_{hp} is the nominal power of the heat pump. The source-side outlet temperature, $T_{hp,S,o}$, and load-side outlet temperature, $T_{hp,L,o}$, are then obtained from standard energy balances:

$$T_{hp,S,o} = T_{hp,S,i} - \frac{Q_{abs}}{c_p \dot{m}_{f,S}}, \tag{5}$$

$$T_{hp,L,o} = T_{hp,L,i} - \frac{Q_{rej}}{c_p \dot{m}_{f,L}}, \tag{6}$$

where $\dot{m}_{f,S}$ and $\dot{m}_{f,L}$ are the mass flow rates through the source and load sides, respectively.

Fig. 3(a) and (b) show the schematic representation of the heat-pump model. The model inputs are the source- and load-side inlet temperatures and mass flow rates, while the outputs are the heat-transfer rate, electrical consumption, and outlet temperatures. The remaining component models, including the water tank, pumps, and heat exchanger, are reported in Appendix A.

3. Case study description

This section defines the case study used to evaluate the integration of a borehole field with a 5GDHC system to provide heating and cooling to residential buildings. The objective is to establish a realistic yet tractable set of parameters and operating assumptions that supports both the short-term verification of component behaviour and the definition of operating-condition boundaries for the subsequent seasonal and system-level analyses. First, the short-term thermal response of the borehole is examined. Next, representative residential heating and cooling demand profiles are introduced for the Barry Island network case study [44,45]. Finally, the short-term operation and efficiency trends of the water-to-water heat pump are assessed under operating conditions representative of 5GDHC systems.

Table 1
Borehole and fluid parameters.

Parameter	Symbol	Value	Unit
Borehole radius	r_g	0.075	m
Pipe outer radius	r_e	0.016	m
Pipe inner radius	r_i	0.013	m
Shank spacing	s	0.030	m
Thermal conductivity of pipe	λ_p	0.39	W/(mK)
Grout thermal conductivity	λ_{gr}	1.528	W/(mK)
Grout specific heat	$c_{p,f}$	2121	J/(kgK)
Grout density	ρ_{gr}	1900	kg/m^3
Fixed mass flow rate of water	$\dot{m}_f$	0.3	kg/s
Density of water	ρ_f	1000	kg/m^3
Dynamic viscosity of water	μ	0.001	kg/(ms)
Specific heat capacity of water	$c_{p,f}$	4180	J/(kgK)
Thermal conductivity of water	λ_f	0.599	W/(mK)

3.1. Borehole performance (Short term)

The composite borehole model used in this work was previously validated in [29] against experimental datasets for boreholes with depths ranging from 6.25 m to 100 m [46,47]. This validation was performed under controlled inlet-fluid-temperature and mass-flow-rate conditions by comparing the simulated and measured outlet temperatures. However, open-access experimental measurements for deeper community-scale systems remain limited. Therefore, an additional controlled verification test was conducted for the present configuration, using defined constant inlet-temperature and mass flow rate conditions to calculate the resulting heat-extraction rate. The simulated extraction rate was then compared with indicative heat extraction ratings reported by the UK installer Kensa [48], including approximately 20 W/m for loose-stone formations. This comparison forms part of the model-validation process and is not intended to represent a time-varying building thermal load.

Three borehole depths were evaluated: 100 m, 150 m, and 200 m. A constant circulating-water mass flow rate of 0.3 kg/s was imposed inside the U-tube to maintain turbulent internal flow. The remaining borehole geometry, grout, and fluid properties were set to typical practical values, as listed in Table 1, while the thermophysical properties of the loose-stone formation are given in Table 2. The initial ground temperature was taken as 13.5 °C. The selected grout thermophysical properties, including thermal conductivity, density, and specific heat capacity, were based on ranges reported in the literature [49,50].

These assumptions provide a benchmark for assessing the short-term heat-exchange capability of the borehole before proceeding to the integrated 5GDHC simulations. Fig. 4 shows the 24 h response for a constant inlet temperature of 4 °C. The 100 m borehole produces an outlet temperature of approximately 6 °C, corresponding to $\Delta T \approx 2$ °C, a

Table 2
Thermophysical properties of loose stones (Saturated Limestone).

Limestone-rich gravel/cobble deposit			
Parameter	Symbol	Value	Unit
Thermal conductivity	λ_{ls}	1.80	W/(mK)
Specific heat	$c_{p,ls}$	1140	J/(kgK)
Thermal diffusivity	α_{ls}	0.75×10^{-6}	$m^2\ s^{-1}$
Density	ρ_{ls}	2100	kg/m^3

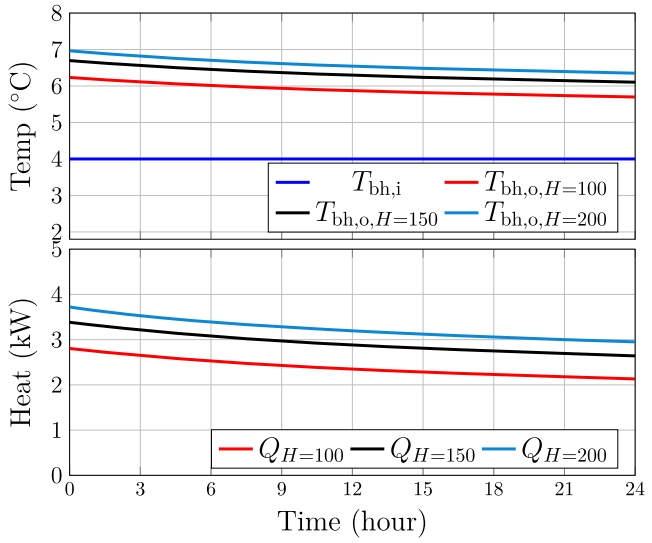


Fig. 4. Short-term borehole response over 24 h for depths of 100, 150 and 200 m ($T_{bh,i} = 4°C$).

mean heat extraction of about 2.38 kW, and a specific extraction rate of 23.87 W/m. The 150 m case yields a similar temperature rise, with a mean heat extraction of 2.92 kW and a specific extraction rate of 19.5 W/m. For the 200 m case, the outlet temperature rise increases to about 2.5 °C, giving a mean heat extraction of 3.23 kW and a specific extraction rate of 16.2 W/m. In all cases, the outlet temperature decreases by approximately 0.5 °C over the 24 h period as the near-borehole region cools under continuous operation. In practice, intermittent demand and variable flow rates would reduce this short-term temperature decay. Overall, the obtained exchange rates are consistent with UK-relevant ranges, approximately 20 W/m, providing confidence for the subsequent integrated simulations.

The Barry Island case study in Wales, UK [44,45], motivated the adoption of a stratified ground profile incorporating an intermediate groundwater-influenced constant-temperature layer. A regional hydrogeological analysis of South Wales by Boon et al. [51] identified a sequence comprising made ground, tidal-flat deposits, glaciofluvial sand and gravel, and Triassic Mercia Mudstone. This regional sequence informed the baseline configuration illustrated in Fig. 5(a), which was simplified for modelling purposes into: (i) a 5 m shallow made-ground layer; (ii) a 25 m intermediate layer representing the tidal-flat and glaciofluvial sand-and-gravel deposits; and (iii) a deeper Mercia Mudstone layer.

The adopted borehole model represents heat transfer through the surrounding ground by conduction and does not explicitly solve advective heat transport caused by groundwater movement. Where groundwater influence is considered, its thermal effect is represented through an idealised temperature-stabilisation condition. The corresponding ground-response sections are maintained close to the undisturbed far-field ground temperature by suppressing their temperature evolution in response to heat exchange with the surrounding soil and grout. This treatment represents a limiting case of strong external thermal exchange

Table 3
Thermophysical properties of soil layers.

Soil type	λ (W/mK)	c_p (J/kgK)	ρ (kg/m^3)	α (m^2/s)
Made ground	1.8	900	1900	1.05×10^{-6}
Soft clay	2.1	850	2400	1.03×10^{-6}
Mudstones	3.0	900	2650	1.26×10^{-6}

and is intended to bound the potential influence of groundwater-induced thermal replenishment on system-level performance; no groundwater mass flow rate, velocity, or flow direction is explicitly imposed. It is therefore not intended to reproduce site-specific groundwater-flow physics. In configuration *u*, this condition is applied only to the designated intermediate groundwater-influenced layer and is referred to here as the partial-groundwater-influenced configuration.

The constant-temperature representation does not explicitly account for groundwater velocity, flow direction, thermal dispersion or asymmetric plume transport. It therefore cannot reproduce upstream-downstream thermal interference or the dependence of borehole-field performance on its orientation relative to the dominant groundwater-flow direction. Furthermore, because the affected layer is assumed to remain close to the undisturbed temperature, the approach may overestimate the stabilising influence of groundwater where the actual advective heat-transfer capacity is limited. The groundwater-related results should consequently be interpreted as idealised bounding scenarios rather than site-specific hydrogeological predictions.

Site investigations undertaken at Barry Waterfront, close to the case-study network, identified a complementary geological sequence in which made ground overlies very soft to soft estuarine silty clay, followed by Mercia Mudstone bedrock in the central and southern parts of the site [52]. This local evidence informed the configuration without groundwater influence illustrated in Fig. 5(b), referred to here as the no-groundwater configuration *v*. The thermophysical properties of the soil layers considered in these configurations are summarised in Table 3.

Finally, an idealised limiting configuration was considered by applying the same constant-temperature representation over the entire borehole depth, referred to here as the full-groundwater configuration *k* (see Fig. 5(c)). This scenario was included to examine the upper-bound effect of groundwater thermal replenishment on stabilising borehole-wall temperatures. The adopted profiles are simplified comparative scenarios and are not intended to reproduce a single site-specific borehole log.

3.2. Thermal network and thermal loads

The case study was based on one branch of the existing Barry Island district heating system described by Liu et al. [44] and Pirouti [45]. For modelling purposes, the central heat source of the fourth-generation district heating system was fictionally replaced by a borehole field, and each connection was represented by a single dwelling or a small shop, according to its use in the original network (Fig. 6). This simplification was introduced to ensure that the annual simulations remained computationally tractable due to the significant number of equations to be solved by the borehole model (see Appendix B). Representing the full-scale buildings using their original heat loads would require a substantially larger borehole field and, consequently, greater computational time. Therefore, representative loads for individual dwellings and small shops were used to maintain realistic operating conditions within a low-temperature district heating and cooling network while limiting the computational burden.

Within this network representation, the dwelling-side temperature targets were set at 45/39 °C supply/return in heating mode and 15/20 °C in cooling mode, corresponding to representative temperature differences of approximately 6 °C and 5 °C, respectively. A reduced network section comprising five dwellings was initially simulated to examine local interactions, as indicated by the shaded area in Fig. 6. The complete branch, comprising six dwellings and six small shops, was sub-

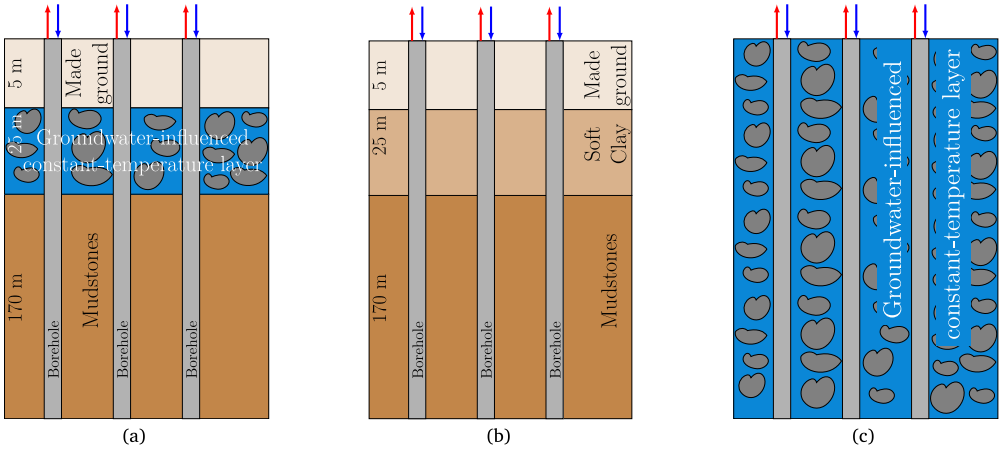


Fig. 5. Ground configurations considered for the Barry Island case study: (a) baseline stratified profile with an intermediate groundwater-influenced layer (u configuration), (b) profile without groundwater influence (v configuration), and (c) idealised groundwater-dominated profile (k configuration).

sequently simulated to assess the scalability of the integrated modelling framework when applied to the full case-study configuration.

Its weekday/weekend structure and inter-dwelling variability were informed by the household heating heterogeneity reported by Hanmer et al. [53] and Pullinger et al. [54]. A representative heating-load scale of approximately 6 kW was adopted, consistent with the value reported by the UK Department for Energy Security and Net Zero [55] for an average property in England. Higher-occupancy dwellings (Houses 1 and 3) reach weekend peaks of approximately 8 kW (see Fig. 7(a) and (e)), whereas the lower-intensity profiles of Houses 4 and 5 peak at approximately 4–5 kW (see Fig. 7(g) and (i)). Cooling operation was introduced from May to September as a prospective scenario, reflecting the emerging importance of residential cooling in a warming climate. The seasonal form of these profiles was informed by the year-round heating and cooling demand profiles for typical British dwellings presented by Corcoran et al. [56]. Although the profiles follow common seasonal trends, their different magnitudes, timing and peak demands represent the diversity of thermal demand among the connected dwellings. Consequently, the aggregated network load accounts for inter-building demand variation rather than assuming an identical thermal profile for every dwelling.

For the system-scale analysis, the complete district leg shown in Fig. 6 comprised six dwellings and six small commercial shops. Commercial demand profiles were included to introduce additional daily and weekly diversity, with some shops operating from Monday to Friday and others from Monday to Saturday. For brevity, only the heating and cooling demand profiles of Shop 1 are presented in Fig. 8. To accommodate the higher aggregated demand, the borehole field was expanded from 8 to 16 boreholes, and the additional main branch was resized to DN65.

The loads were linked to the water-tank interface by imposing fixed return temperatures, T_{ret}, of 39 °C in heating mode and 20 °C in cooling mode, with target supply temperatures, T_{sup}, of 45 °C and 15 °C, respectively. These temperatures were imposed as boundary conditions at the buffer-tank interface rather than calculated using a dynamic building-envelope model. A time-varying thermal demand can be represented either by varying the temperature difference at a constant mass flow rate or by varying the mass flow rate at a defined temperature difference. The latter approach was adopted in this study. This variable-flow representation is consistent with the CIBSE Design Guide: Heat Networks, which addresses the control of water flow rates and operating temperatures in hydronic networks and notes that the same principles can also be applied to cooling networks [57]. The instantaneous demand was then implemented by modulating the tank-side mass flow rate according to

$$\dot{m}_f = \frac{Q}{c_p \Delta T}, \tag{7}$$

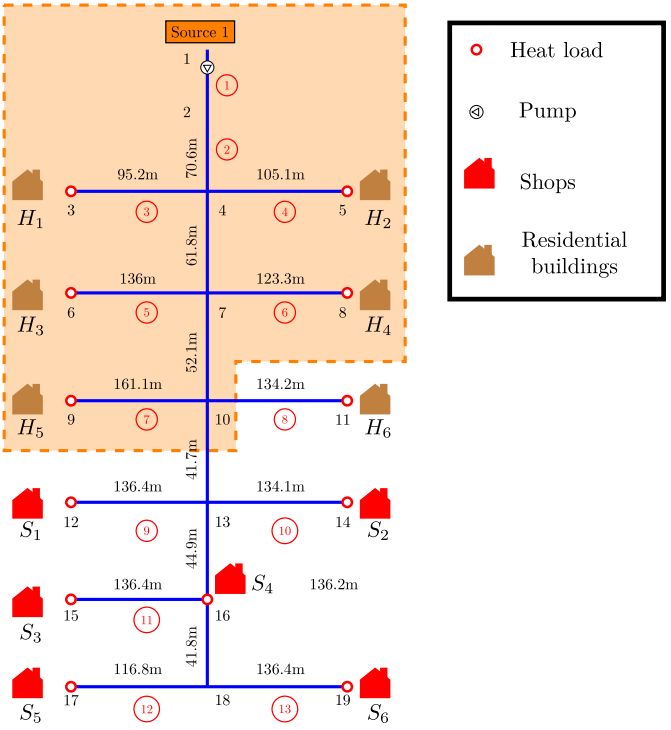


Fig. 6. One leg of the Barry Island district system used as the basis for the 5GDHC retrofit case study.

where Q (W) is the thermal demand, c_p is the specific heat capacity of water, and $\Delta T = T_{sup} - T_{ret}$. The defined temperature differences were therefore 6 °C in heating mode and 5 °C in cooling mode. Consequently, the temporal variation of each demand profile was transferred to the hydraulic model through the corresponding variation in the tank-side mass flow rate. Fig. 9 shows the resulting combined signed load, where positive values denote heating and negative values denote cooling.

3.3. Heat pump performance (Short term)

The decentralised water-to-water heat pumps must satisfy the building supply-temperature targets while maintaining acceptable source-side operating conditions. The selected unit is representative of a residential-scale water-to-water heat pump, with a rated heating capacity of 6 kW and nominal source- and load-side mass flow rates of 0.33 kg/s. In heating mode, excessive source-side temperature drops re-

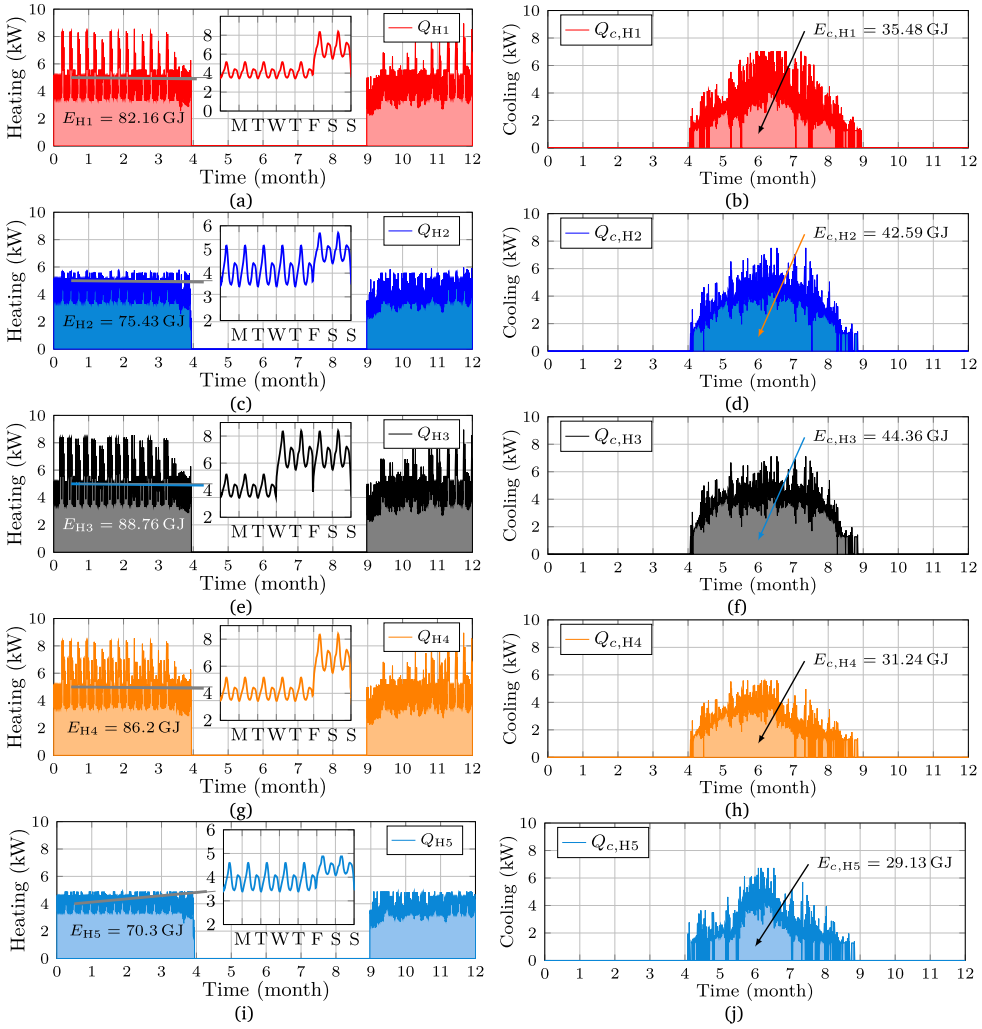


Fig. 7. Heating demand profiles: (a) House 1, (c) House 2, (e) House 3, (g) House 4 and (i) House 5. Cooling demand profiles: (b) House 1, (d) House 2, (f) House 3, (h) House 4 and (j) House 5.

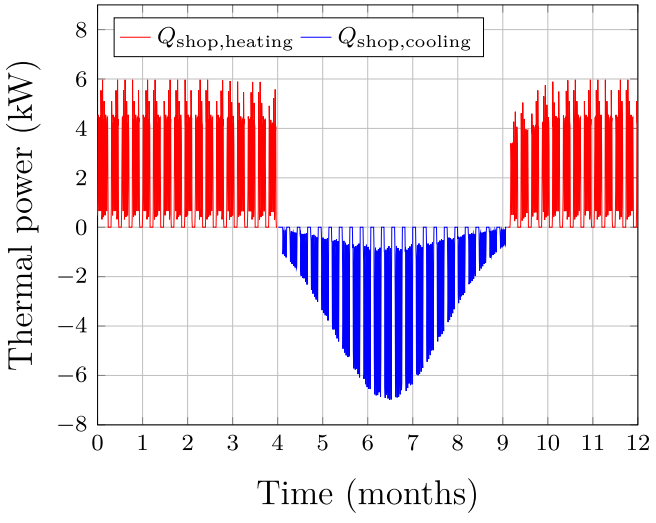


Fig. 8. Typical aggregated heating and cooling demand profiles for small shops with commercial schedule of Monday–Friday.

duce the evaporating temperature, lower the COP, and increase the risk of freezing. To limit this effect, a reference source-side temperature difference of $\Delta T_S = 6$ °C was adopted.

The buffer tank temperature was regulated using an on/off control strategy adapted from [39], with a hysteresis band of ±2 °C around the heating or cooling set-point (Fig. 10). On the demand side, the circulation pump tracks the required tank-side mass flow rate through an open-loop proportional controller to satisfy the imposed building load. On the source side, a higher proportional gain was used to limit deviations in ΔT_S and ensure sufficient network-side flow through the heat pump. Because the heat pump is represented by non-linear performance maps, the controller gains were tuned heuristically to achieve stable behaviour without excessive oscillations.

Representative one-week simulations confirm that the intended control behaviour is achieved. During the heating season for House 1, the tank supply temperature, T_{sup}, remains close to 45 °C, with only minor reductions observed during periods of higher weekend demand (Fig. 11(a), (b)). The network-side heat exchanger operates with a temperature difference of approximately 2.6 °C, defined as the difference between the inlet and outlet temperatures, $T_{HE,S,i}$ and $T_{HE,S,o}$, while the heat-pump source circuit maintains $\Delta T_S \approx 6$ °C (Fig. 12(a)–(c)). This behaviour supports efficient operation and limits excessively low return temperatures to the borehole loop. During cooling operation, the supply-temperature target is also achieved despite lower and more variable loads. Although the heat exchanger then experiences larger temperature drops due to reduced mass flow rates (Fig. 11(c), (d)), the source-side temperature difference remains bounded, indicating effective control (Fig. 12(d)–(f)). Further details of the heat-pump model and the

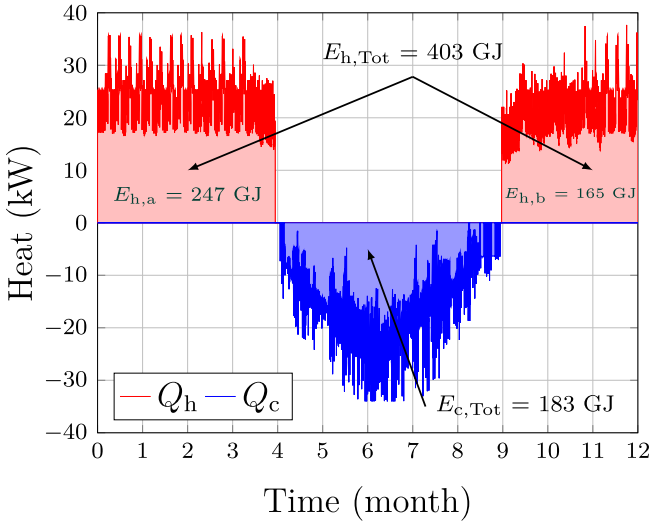


Fig. 9. Combined signed thermal demand of the five dwellings (positive: heating; negative: cooling).

heating and cooling performance curves employed in the simulations are provided in Appendix C.

4. Simulation results

This section evaluates the coupled behaviour of the borehole field and the 5GDHC system under the residential heating and cooling demands introduced in Section 3. The integrated system was simulated in TRNSYS over one year for three ground representations and four heating-to-cooling ratios. The analysis focuses on: (i) borehole-field inlet and outlet temperatures, (ii) soil-layer temperature evolution, (iii) the ability of the building interfaces to satisfy the required supply temperatures, and (iv) heat-pump performance through COP and SCOP calculations. The results are presented in this order to clarify how ground-side thermal behaviour propagates through the network and ultimately affects end-use performance and seasonal efficiency.

4.1. Ground-side thermal response of the borehole field

The borehole layout adopted for the integrated simulations consists of one central borehole surrounded by seven equally spaced boreholes (Fig. 13). The adopted 4 m spacing represents a deliberately compact case-study configuration selected to reflect the restricted ground availability that may arise in urban 5GDHC implementations, rather than a generally representative or optimal borehole spacing. The influence of borehole spacing is further assessed in Appendix D through additional simulations considering spacings of 5, 6, and 8 m in comparison with the original 4 m configuration. Although this layout does not produce the highest outlet temperature among the candidate arrangements, Appendix E shows that it provides a more uniform temperature evolution along the borehole depth. In addition, Appendix B shows the effect of the selected nodal discretisation on the representation of the stratified soil layers. The maximum outlet-temperature difference relative to the best-performing layout is only about 0.2 °C. Therefore, this geometry was selected because it provides a balanced borehole-field response for the integrated simulations.

Fig. 14 first presents the results for configuration k, which represents an idealised full-depth constant-temperature condition. During the heating season, the borehole outlet temperature, $T_{bh,o,k}$, remains close to 11 °C, while the inlet temperature, $T_{bh,i,k}$, remains near 8 °C. During the cooling season, the outlet temperature is approximately 20.7 °C, while the return temperature is about 14.5 °C. In both seasons, the borehole supply–return temperature difference remains below 6 °C. The mass flow rate through the system, $\dot{m}_{f,k}$, is largely demand-driven: it remains close to 1.65 kg/s during the heating season and varies between approximately 0.6 and 1.37 kg/s during cooling, as the cooling demand increases and then declines.

Fig. 15 shows the results for borehole configuration u, which represents the layered South Wales ground profile with one groundwater-influenced layer. In contrast to configuration k, both the inlet temperature, $T_{bh,i,u}$, and outlet temperature, $T_{bh,o,u}$, now evolve seasonally. During the first heating season, the outlet temperature decreases from 10.9 °C to 8.2 °C, while the inlet temperature decreases from 7.5 °C to 5.3 °C. During cooling, the outlet temperature increases from about 12.3 °C to around 13 °C, while the inlet temperature rises from 18.6 °C to approximately 20 °C. Unlike configuration k, the start of the following heating season occurs at slightly higher temperatures than those reached at the end of April, indicating partial thermal recharge during summer. The mass flow rate, $\dot{m}_{f,u}$, remains almost unchanged relative to configuration k, confirming that the flow is controlled mainly by building-side demand rather than by the soil configuration.

The behaviour of configuration u is better understood from the soil-node temperatures shown in Fig. 16; Appendix B provides the reference for the layer-node definitions (two nodes for each layer). The thin made-ground layer exhibits the sharpest response to heat extraction, particularly at node $T_{b,L1,2,u}$, which decreases to about 4.5 °C. By contrast, the deeper mudstone nodes remain warmer, with minimum temperatures around 8 °C, because of their larger thermal mass. During cooling, all active nodes warm up, with the largest increases occurring at $T_{b,L1,2,u}$ and $T_{b,L3,2,u}$. Overall, the figure shows that summer heat rejection partly restores the subsurface thermal state.

The strongest thermal depletion occurs in configuration v, where the groundwater-influenced layer was replaced by soft clay. As shown in Fig. 17, the inlet temperature, $T_{bh,i,v}$, falls to 3.8 °C by the end of the first heating season, while the outlet temperature, $T_{bh,o,v}$, reaches a minimum of approximately 6.2 °C. During the cooling season, the outlet temperature rises to around 11.8 °C, but the system starts this season from a colder state than in configurations k and u. After summer, both supply and return temperatures increase, indicating partial thermal recovery; however, the start of the subsequent heating season remains below the corresponding values in the other two configurations. No significant changes in mass flow rate are observed compared with configurations k and u, confirming that regulation is primarily determined by heat-pump operation rather than by the ground-layer configuration.

Fig. 18 confirms that configuration v produces greater thermal depletion in the deeper layers, particularly in the mudstone layer, where node 1, $T_{b,L3,1,v}$, reaches a minimum value of about 7.5 °C. This is 0.7 °C lower than the corresponding value in configuration u, indicating stronger net seasonal heat extraction from the soil. Figs. 14–18 show a clear ranking of thermal stability: configuration k is the most stable, configuration u exhibits moderate seasonal depletion with partial recharge, and configuration v experiences the largest seasonal drift. Importantly, the borehole-field mass flow rate remains similar across all cases. Therefore, the main difference between configurations lies in the supply temperature available to the decentralised heat pumps, whereas the network hydraulic behaviour, represented by the mass flow rate, remains essentially unchanged.

Note: The pronounced temperature variations during the first year are primarily associated with the initial thermal transient following the start of borehole-field operation. These variations decrease over time as the soil-layer temperatures progressively stabilise. After the initial year, the annual depletion of the borehole-field outlet temperature is reduced to approximately 0.3 °C. Further details are provided in the Discussion section.

4.2. Building-side temperature delivery and heat-pump operation

Fig. 19 presents the buffer-tank supply temperature for House 1, T_{H1}, under the three borehole configurations. In heating mode, the controller

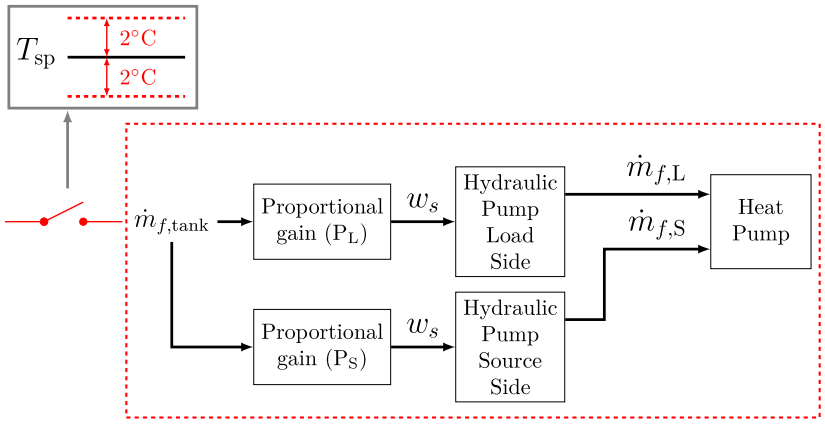


Fig. 10. Load and source side control structure: tank temperature on/off logic and demand-driven circulation. **Note:** Nonlinear heat-pump control design is a challenging task; gains were tuned heuristically to ensure stable operation.

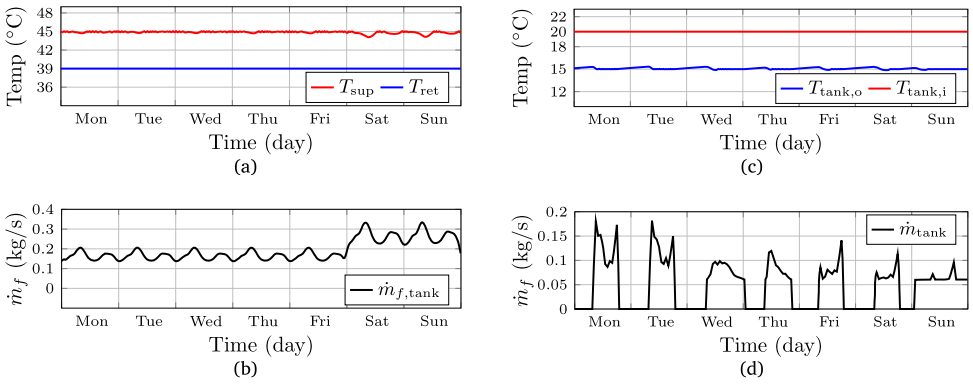


Fig. 11. House 1 thermal demand conditions: building supply/return temperatures and demand-side tank mass flow rates for (a,b) heating and (c,d) cooling modes.

maintains the 45 °C set-point throughout the season, with only short-duration drops of up to about 2 °C during peak demand periods. In cooling mode, the 15 °C set-point is also maintained, with deviations generally below 1.5 °C. The three temperature traces almost overlap, indicating that the decentralised control strategy can reject moderate variations in network temperature and preserve the required service level.

The same behaviour is observed for the remaining dwellings (Fig. 20). Houses with lower thermal demand, such as Houses 2 and 5, show the smallest deviations from the set-point, while Houses 3 and 4 exhibit slightly larger drops during peak heating periods. Nevertheless, all dwellings remain within the controller dead band, and cooling-season deviations remain small even around the summer peak. These results demonstrate that all three borehole representations provide acceptable thermal performance at the building level.

The mass flow rate, $\dot{m}_f$, through the heat-exchanger interface for House 1 is shown in Fig. 21. During heating, the flow profiles are almost identical for configurations k, u, and v, confirming that the control strategy is primarily load-driven. During cooling, configuration v produces a slightly lower flow rate because the colder source side increases the temperature difference across the heat exchanger, allowing the same cooling duty to be delivered with marginally less circulation. However, these differences are small, indicating that the network hydraulics are only weakly sensitive to the soil configuration under the adopted control strategy.

Fig. 22 presents the instantaneous COP of the heat pump for House 3, which has the most demanding heating profile. In heating mode, the COP remains broadly between 4.5 and 5.0 for all three cases, indicating that the moderate differences in borehole supply temperature do not strongly affect instantaneous heating performance at the building side. In cooling mode, configuration k yields the highest COP because the groundwater-stabilised thermal boundary reduces the effective temperature lift. Configurations u and v begin the cooling season from colder ground states and therefore show slightly lower cooling COP values. Fig. 23 supports this interpretation by separating heat-pump and pump electricity consumption. Here, the subscripts hp, m, p, and s denote the heat pump, main hydraulic pump, primary hydraulic pump, and secondary hydraulic pump, respectively (see Fig. 1). Configuration k tends to reduce compressor power slightly, whereas pump power remains similar across cases, confirming that the main source of performance variation is the thermal state of the borehole rather than building-side hydraulics.

4.3. Seasonal efficiency and the role of summer recharge

Table 4 summarises the seasonal coefficient of performance for the baseline case. The annual SCOP is highest for configuration k (3.69), followed by configurations u (3.54) and v (3.45). This ranking is consistent with the ground-side analysis: the more stable the borehole temperature, the higher the seasonal heat-pump efficiency. However, the differences remain small, showing that decentralised controls and buffer tanks attenuate part of the thermal variability before it reaches the building supply level. The same trend is observed when separating the first heating season, $SCOP_a$, from the post-summer heating season, $SCOP_b$; the latter is more sensitive to the degree of thermal recovery achieved during cooling.

To assess the value of seasonal charging more explicitly, the summer cooling demand was reduced to 0, 50, 75, and 100% of the baseline cooling load. Fig. 24 shows the outlet temperature, T_o, of the borehole field under different cooling demands. Configuration k is essentially insensitive to this change because the established constant-temperature boundary keeps the borehole temperature nearly fixed. By contrast, con-

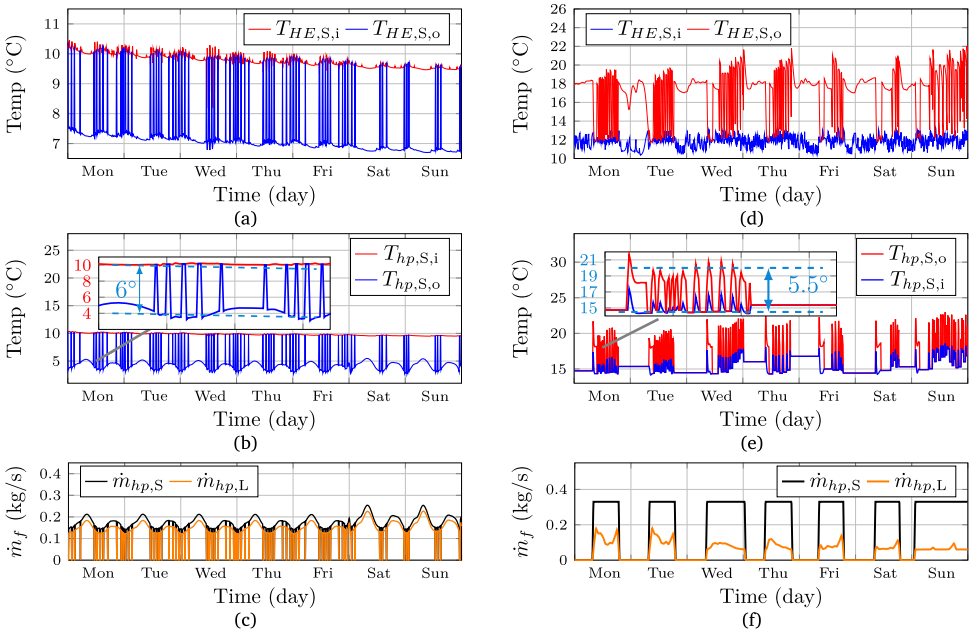


Fig. 12. Heat-pump operating conditions over one week: heat-exchanger inlet/outlet temperatures, source-side inlet/outlet temperatures, and source/load mass flow rates for (a–c) heating and (d–f) cooling modes.

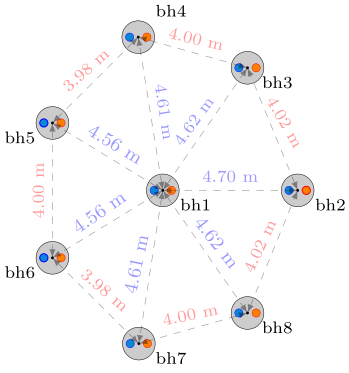


Fig. 13. Selected borehole-field layout: one central borehole surrounded by seven equally spaced boreholes.

Table 4
SCOP for the three soil configurations in the baseline case.

Soil layer configuration	$SCOP_T$	$SCOP_a$	$SCOP_b$
k	3.69	3.88	3.65
u	3.54	3.72	3.51
v	3.45	3.63	3.41

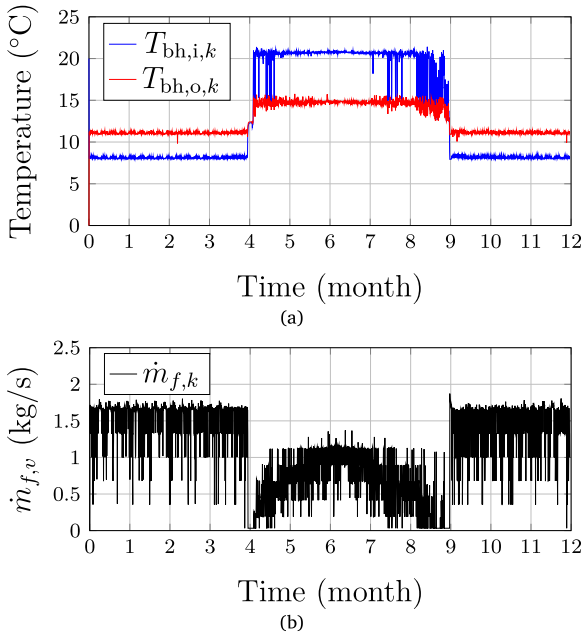


Fig. 14. Configuration k: (a) borehole-field inlet and outlet temperatures; (b) mass flow rate through the borehole field.

figurations u and v respond clearly to reduced cooling-season heat rejection. Lower summer charging leads to lower borehole temperatures at the start of the next heating season, with a stronger effect observed for configuration v. This indicates that, where the ground is not thermally stabilised by groundwater, summer operation affects the thermal state available for the following winter.

The SCOP values in Table 5 confirm the same pattern. $SCOP_a$ remains unchanged because all cases start from the same initial ground condition, whereas $SCOP_b$ decreases as cooling-season charging is reduced. The largest decrease occurs in configuration v, followed by configuration u, while configuration k remains unchanged. Therefore, the benefit of seasonal borehole charging depends strongly on the thermal recovery characteristics of the site and on the balance between winter heat extraction and summer heat rejection. This result is particularly relevant for residentially dominated 5GDHC systems, where heating loads may substantially exceed cooling loads.

The resulting SCOP values are also consistent with the ranges reported in previous studies of water-to-water and ground-source heat-pump systems [58,59], supporting the realism of the predicted seasonal performance.

4.4. Extended district-leg analysis

To assess scalability, this subsection presents the simulation results obtained for the extended district-leg configuration defined in the Case study description section. The analysis evaluates system performance

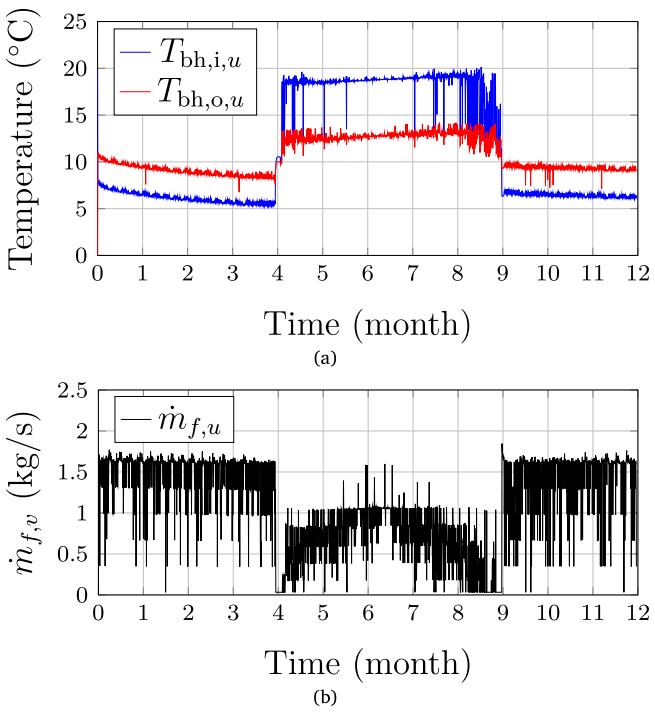


Fig. 15. Configuration u: (a) borehole-field inlet and outlet temperatures; (b) mass flow rate through the borehole field.

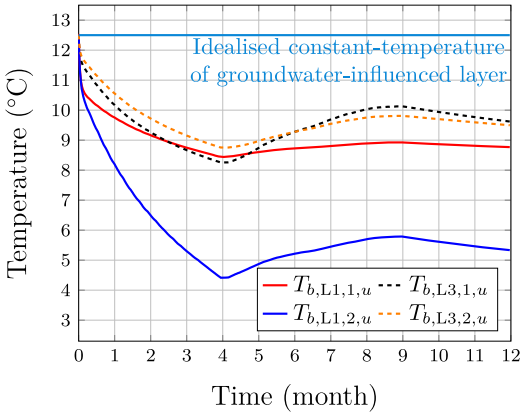


Fig. 16. Configuration u: soil-node temperatures in the made-ground and mudstone layers; the groundwater-influenced layer is represented an idealised constant temperature condition of 12.5 °C.

Table 5
SCOP under different cooling-charge levels.

Config.	Cooling charge (%)	$\mathrm{SCOP_T}$	SCOP_a	SCOP_b
k	0, 50, 75, 100	3.69	3.88	3.65
u	0	3.50	3.72	3.41
	50	3.53	3.72	3.46
	75	3.54	3.72	3.50
	100	3.54	3.72	3.51
v	0	3.39	3.63	3.27
	50	3.44	3.63	3.37
	75	3.45	3.63	3.41
	100	3.45	3.63	3.41

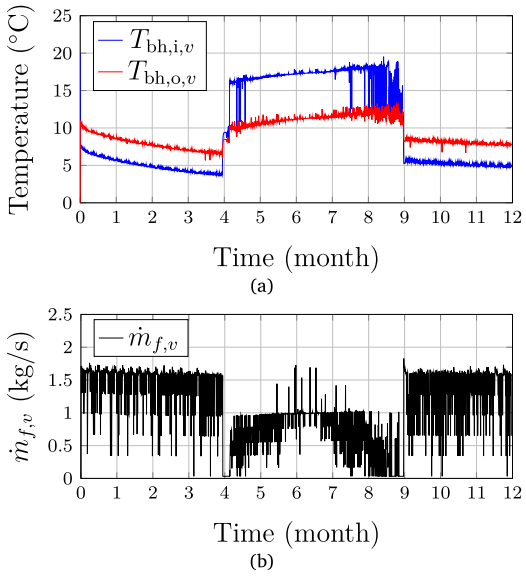


Fig. 17. Configuration v: (a) borehole-field inlet and outlet temperatures; (b) mass flow rate through the borehole field.

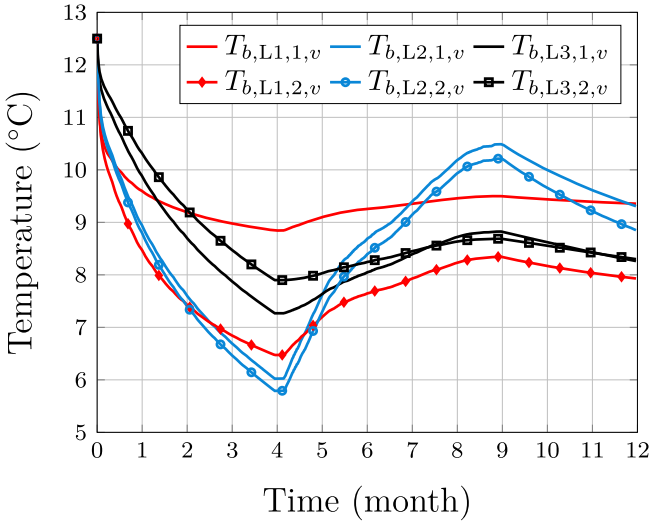


Fig. 18. Configuration v: soil-node temperatures in the made-ground, soft-clay, and mudstone layers.

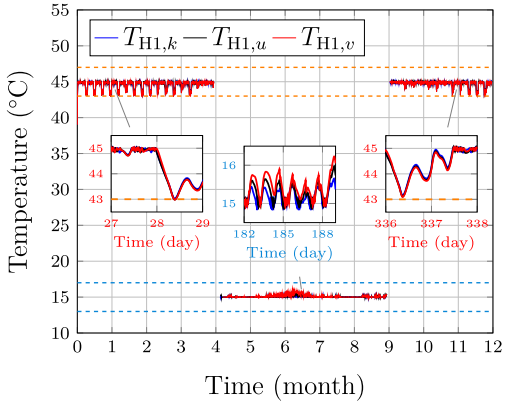


Fig. 19. House 1 buffer-tank supply temperature under borehole configurations k, u, and v.

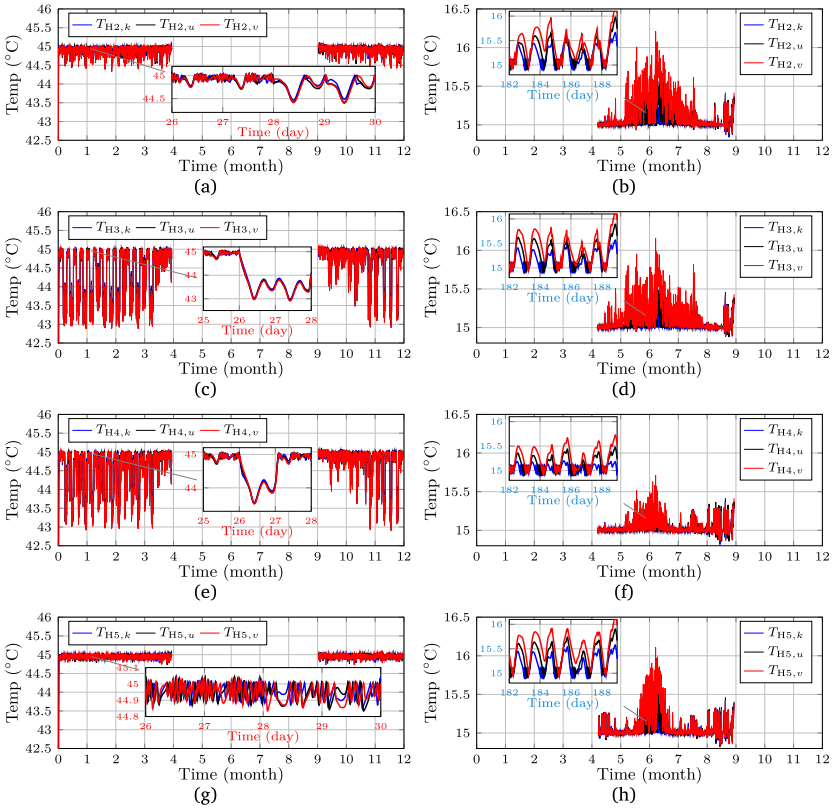


Fig. 20. Supply temperature delivered to Houses 2–5 under borehole configurations k, u, and v.

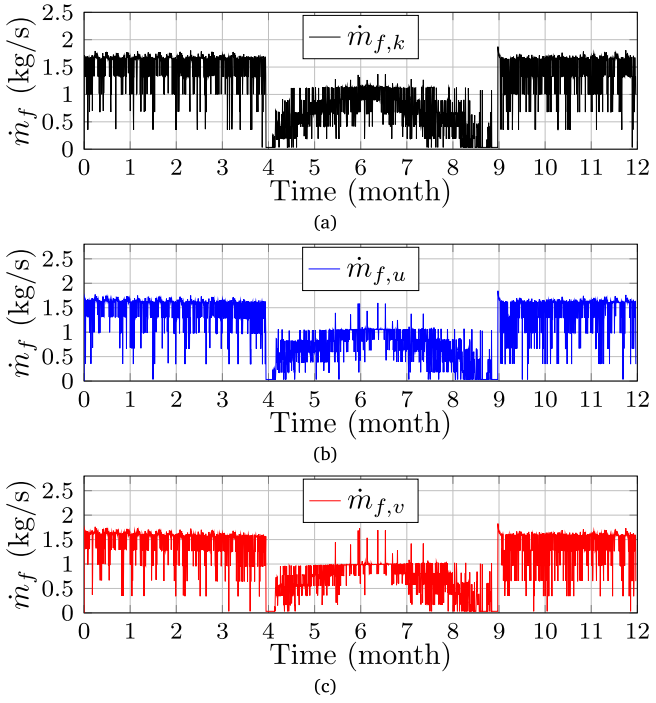


Fig. 21. House 1 mass flow rate through the heat-exchanger interface for borehole configurations: (a) k, (b) u, and (c) v.

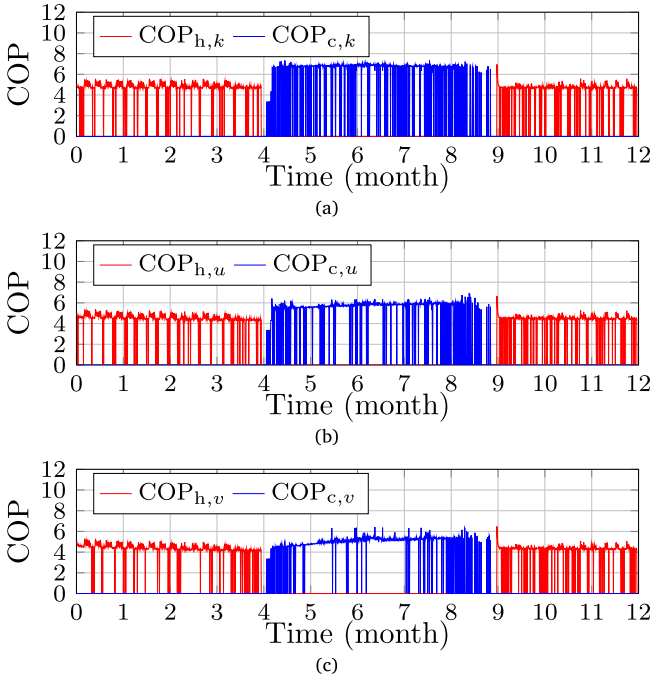


Fig. 22. Heat-pump COP for House 3 under borehole configurations: (a) k, (b) u, and (c) v.

under the increased and diversified demand of the complete network using the corresponding borehole-field and pipe-sizing assumptions established previously.

Given space limitations in the discussion of the extended case study, only the most conservative ground condition, namely configuration v, was selected. Even under this no-groundwater assumption, the borehole field remains capable of supplying the network without reaching critically low temperatures during heating operation (see Fig. 25). Although the larger and more diverse demand increases short-term variability, the decentralised heat pumps continue to satisfy the required supply-temperature set-points across the connected dwellings and shops.

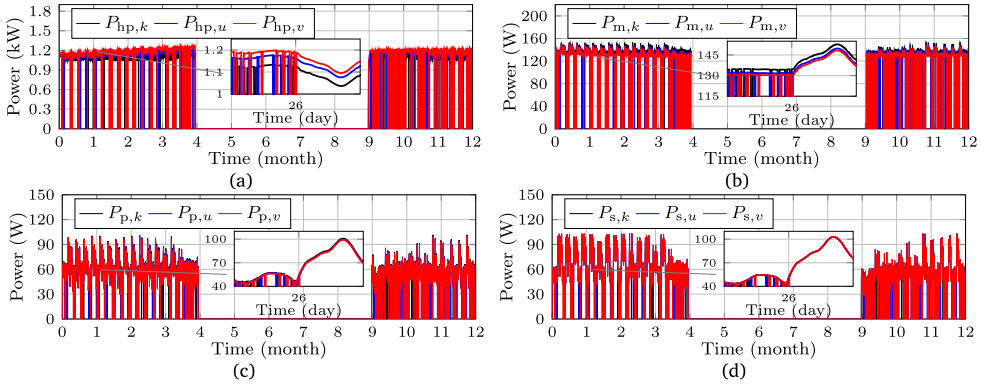


Fig. 23. Electrical power consumption for House 3: (a) heat-pump compressor and circulation pumps ((b) main pump, (c) primary pump and (d) secondary pump) for configurations k, u, and v.

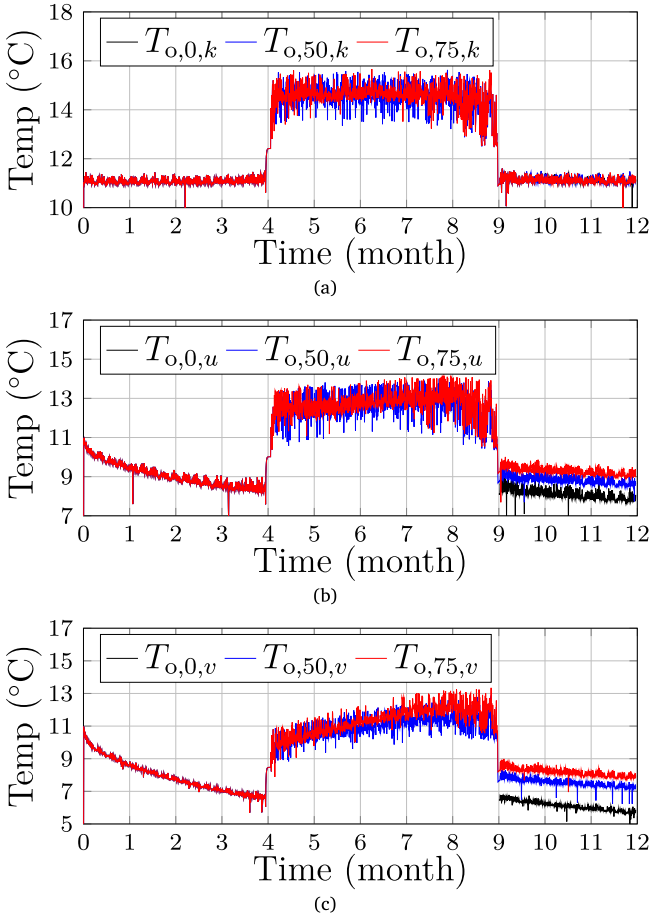


Fig. 24. Borehole-field temperatures under different summer cooling-charge levels for configurations: (a) k, (b) u, and (c) v.

This final test therefore indicates that the coupled borehole–5GDHC framework remains operational when the system is scaled beyond the reduced residential case, while also confirming that the no-groundwater configuration provides a useful conservative bound for design assessment.

5. Discussion

The results indicate that integrating a fifth-generation district heating and cooling (5GDHC) network with a borehole field and decentralised water-to-water heat pumps is technically feasible for the case study considered. The simulations show that the required building supply temperatures can be maintained while operating with source temperatures consistent with residential-scale water-to-water heat pumps. However, the extent to which these findings can be generalised depends on four practical factors: soil characterisation, heat-pump performance, retrofit requirements in existing dwellings, and the annual heating-to-cooling ratio.

Soil characterisation is the first major source of uncertainty because soil properties and groundwater flow directly govern borehole heat exchange and long-term thermal recovery. Errors in the assumed ground layering, thermal conductivity, heat capacity, or groundwater influence propagate into the predicted borehole temperatures and, consequently, into COP and SCOP estimates. This effect is evident in the comparison between configurations k, u, and v: the groundwater-influenced constant-temperature case maintains the highest and most stable temperatures, whereas the no-groundwater case experiences the strongest thermal depletion. In practice, borehole logs, thermal response tests, and hydrogeological assessments would be required to reduce this uncertainty and better constrain layered ground models.

A second important factor is the heat-pump performance adopted in the simulations. The performance maps used here show only moderate COP variation over the source-temperature range considered, leading to relatively stable temperature differences across the heat pump. This moderates the thermal stress imposed on the borehole field and helps explain the gradual variation in $T_{bh,o}$ during heating and after summer recharge. Therefore, ground thermal evolution depends not only on the net extracted and injected loads but also on how strongly the heat-pump operating point changes with source-side conditions. In the present case, the assumption of a constant load-side inlet temperature of 39 °C contributed to this stable behaviour.

The adopted COP range is also consistent with the literature. Bilardo et al. [60] reported COP values between 3.4 and 3.7 for water-to-water heat pumps in a 5GDHC system with source inlet temperatures between 5 and 10 °C. Viviescas et al. [61] reported COP values between 4.0 and 4.3 for source temperatures between 10 and 15 °C, while Ohtani et al. [62] showed similarly small COP variations with source temperature. Comparable values were also reported by Emmi et al. [58,59]. These studies support the realism of the heat-pump representation adopted here.

Third, retrofit requirements remain an important limitation for application in the existing housing stock. Even when the borehole field and ambient loop provide suitable source temperatures, many dwellings would still require an interface substation, low-temperature emitters, and, in some cases, fabric improvements or emitter upgrades. Domestic hot-water provision may introduce additional complexity through storage, pasteurisation, or auxiliary electric boosting, thereby increasing electricity demand and affecting both network and borehole operation. The present results should therefore be interpreted

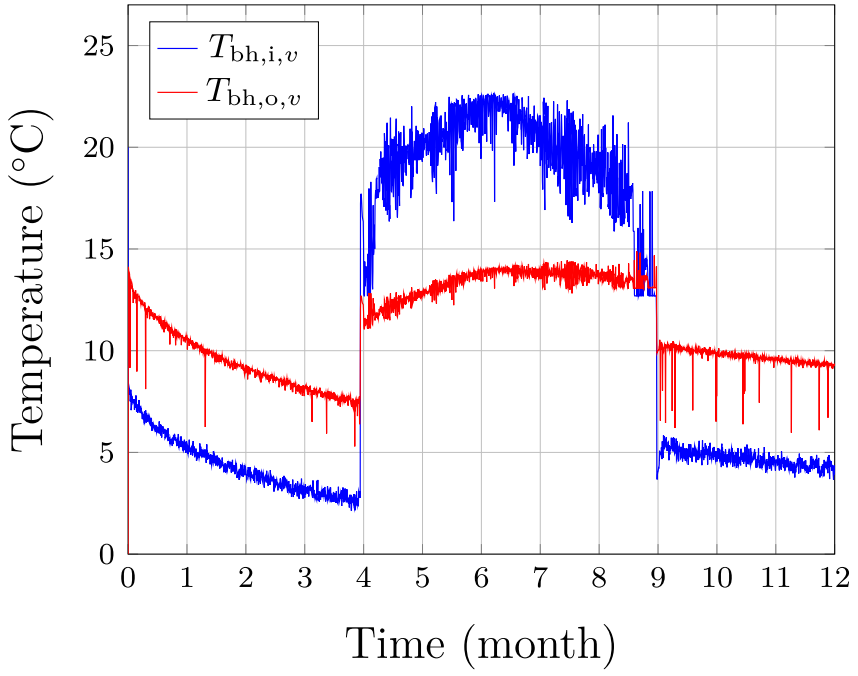


Fig. 25. Borehole field inlet and outlet temperatures for whole district heating system with 6 residential buildings and 6 shops.

as evidence of system-level feasibility under the assumed building-side conditions, rather than as being directly applicable to all existing homes.

The most critical issue for long-term operation is the annual heating-to-cooling ratio. To examine its effect, balanced and unbalanced conditions were compared using the no-groundwater configuration, v. The balanced case was created by imposing a hypothetical constant cooling demand so that the annual heating-to-cooling ratio became 1:1, meaning that winter heat extraction was approximately offset by summer heat injection. Fig. 26 shows the resulting balanced load profile.

The effect of this balance becomes clear in Fig. 27. Under heating-dominated operation, with a heating-to-cooling ratio of 2.1:1, the borehole field exhibits progressive thermal drift over three years. Although the largest temperature variation occurs during the initial year of operation, the annual depletion of the borehole-field outlet temperature subsequently decreases to approximately 0.3 °C (see Fig. 27). This reduced rate is associated with the progressive stabilisation of the soil-layer temperatures shown in Fig. 28 and supports the potential for an extended operating lifetime. Nevertheless, the continuing downward trend confirms that the imbalance between heat extraction and injection still affects long-term thermal performance. If maintained over longer periods, this imbalance would increase the likelihood of approaching freezing conditions near the borehole.

By contrast, the balanced case remains much more stable. In Fig. 27(b), $T_{\mathrm{bh,o},r}$ remains close to its initial value of about 10.5 °C after the first charging season, while $T_{\mathrm{bh,i},r}$ stays near 7.5 °C. This shows that, when summer heat injection offsets winter heat extraction, the borehole field can maintain acceptable thermal conditions and long-term drift is substantially reduced.

The same conclusion is supported by the soil-node temperatures in Fig. 28. Under balanced operation, the node temperatures remain approximately stable after the first annual cycle. Under heating-dominated operation, the soil-layer temperature variations become substantially smaller after the initial year, indicating that the borehole field progressively approaches a more stable thermal regime. However, the deeper nodes continue to decline gradually, demonstrating that thermal stabilisation does not eliminate the cumulative effect of the annual energy imbalance.

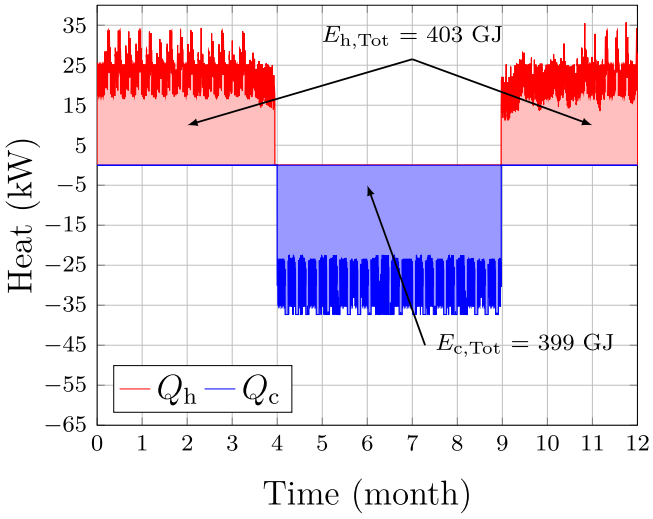


Fig. 26. Combined signed thermal demand used to impose the balanced case with a heating-to-cooling ratio of 1:1.

An additional practical consideration is the response of the system during periods of high aggregated heating demand or progressive reduction of the borehole-field temperature. In the present configuration, a central heat pump is not required to maintain the building supply temperature because the temperature lift is provided by the decentralised water-to-water heat pumps. Consequently, a reduction in the borehole outlet temperature reduces the temperature available to the decentralised water-to-water heat pumps at the building substations, increasing the required temperature lift and electrical consumption and ultimately reducing their COP. Within the operating range investigated here, including the extended district-leg case with six dwellings and six shops, for which the borehole-field capacity was increased to accommodate the higher aggregated heating demand, and the conservative no-groundwater configuration, the decentralised heat pumps remained capable of maintaining the required building supply-temperature set-

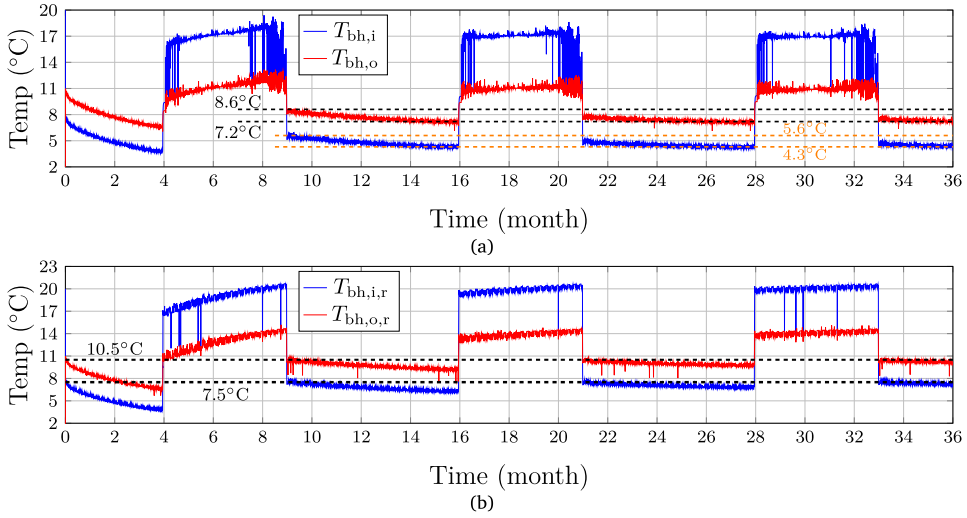


Fig. 27. Three-year borehole-field temperatures for the no-groundwater configuration: (a) heating-dominated operation; (b) balanced operation after seasonal recharge.

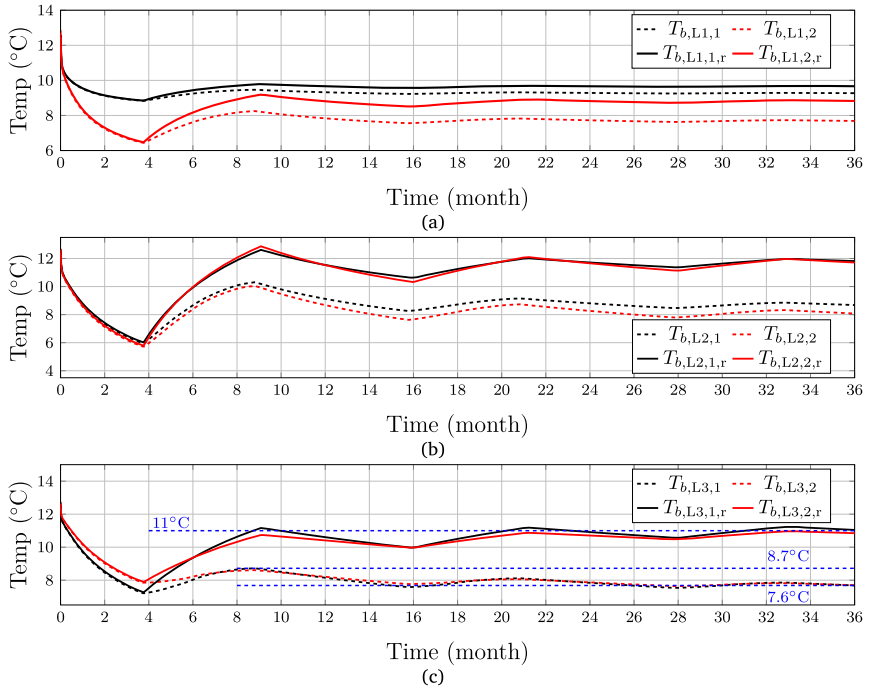


Fig. 28. Three-year soil-node temperature evolution for the no-groundwater configuration under balanced and heating-dominated operation: (a) Layer 1, (b) Layer 2, and (c) Layer 3.

points without the borehole field reaching critically low temperatures. However, this result should not be interpreted as implying unlimited heat-extraction capability. If higher peak loads beyond the design conditions were to reduce the borehole temperature below the admissible operating range of the decentralised water-to-water heat pumps, additional thermal input, load management, increased borehole capacity, or an auxiliary heat source would be required.

Overall, the results suggest that the long-term value of borehole thermal storage in 5GDHC systems depends less on short-term feasibility, which was achieved in all simulated cases, and more on whether the annual energy balance allows the ground to recover. The reduced outlet-temperature depletion after the initial year indicates the potential for extended operation; however, maintaining a suitable balance between heat extraction and injection remains essential for limiting long-term thermal drift. In practice, this balance may be improved not only by space-cooling demand, but also by solar-assisted charging, low-grade waste-heat recovery, or operational strategies that promote summer heat injection. For heating-dominated residential networks, the heating-to-cooling ratio should therefore be treated as a key design and operational parameter.

6. Conclusions

This paper developed and applied an integrated modelling framework to evaluate seasonal borehole heat exchangers (BHEs) within a fifth-generation district heating and cooling (5GDHC) network supplying decentralised water-to-water heat pumps. The framework, implemented in TRNSYS, simulates both short-term operation and seasonal interactions between the borehole field, the bidirectional low-temperature network, building-level substations, and residential heating and cooling

demands. In this way, the study links hourly operational behaviour with the longer-term thermal evolution of the ground.

A real network layout in Barry Island, Wales, was used as the case study, with the existing thermal source replaced by a borehole field coupled to decentralised heat pumps. The results confirmed strong thermal coupling between the ground and the network. The borehole supply temperature was governed by the aggregated network return temperature, while the network return temperature was shaped by local heat-pump operation, control strategy, and source-side conditions. Despite this coupling, the decentralised water-to-water heat pumps were able to maintain the required building supply temperatures in both heating and cooling modes, showing that local control can provide effective energy management within a low-temperature 5GDHC architecture.

The comparison of the three soil configurations showed that subsurface conditions strongly influence borehole-field behaviour. The idealised groundwater influenced, temperature-stabilised configurations produced the most stable borehole temperatures, whereas the no-groundwater influenced temperature case exhibited the strongest seasonal depletion. Nevertheless, the three-year simulation of this most unfavourable configuration showed that the pronounced first-year thermal response was followed by an annual borehole-field outlet-temperature depletion of approximately 0.3°C. This reduced rate coincided with progressively smaller variations in the soil-layer temperatures, indicating partial thermal stabilisation after the initial operating year and the potential for an extended operating life. However, the continuing downward trend under heating-dominated conditions confirms that the annual imbalance between heat extraction and injection still affects long-term performance. The results also showed that the borehole field can operate both as a short-term source/sink and as a seasonal thermal store. Heat rejected during the cooling season partially recharged the ground and increased the source temperature available for the following heating season. This seasonal benefit was modest under the baseline loads but became more evident when the heating-to-cooling ratio was varied.

Heat-pump COP and SCOP remained within realistic ranges and showed only moderate sensitivity to the source-temperature variations predicted in the simulations. This indicates that the proposed concept is technically robust under the operating conditions considered. However, the results also highlighted the importance of local control. Regulating the mass flow rate to maintain bounded source-side temperature differences was essential to avoid excessive thermal depletion, preserve heat-transfer capacity, and satisfy building loads.

Overall, the study shows that integrating BTES with a 5GDHC network and decentralised water-to-water heat pumps is technically feasible. However, its long-term performance depends on appropriate heat-pump performance over the expected operating range, effective decentralised control, and a sufficiently balanced annual heating-to-cooling ratio. Although the reduced depletion after the initial year supports the potential for extended operation, it does not eliminate the cumulative effect of a persistent thermal imbalance. For residentially dominated systems, where heating demand exceeds cooling demand, supplemental summer charging is likely to be required to avoid long-term thermal drift in the borehole field.

Future work should therefore focus on alternative charging strategies, including solar-assisted heat injection and the recovery of low-grade waste heat, together with techno-economic assessment. In addition, incorporating the dynamic thermal behaviour of residential buildings would improve the accuracy of the analysis by providing a more realistic representation of interactions with building demand. These aspects are needed to quantify the operational and lifecycle value of seasonal BTES in practical 5GDHC deployments.

CRediT authorship contribution statement

Hector Bastida: Writing – original draft, Visualization, Validation, Software, Methodology, Investigation, Formal analysis, Conceptualization; **Meysam Qadrdan:** Writing – review & editing, Supervision, Project administration, Methodology, Funding acquisition, Formal analysis, Conceptualization; **Wu Gao:** Writing – review & editing, Software, Methodology, Formal analysis.

Declaration of competing interest

The authors declare that they have no known competing financial interests or personal relationships that could have appeared to influence the work reported in this paper.

Acknowledgements

The work presented in this paper was supported by UK Research and Innovation (UKRI) through the Energy Demand Research Centre, Grant EP/Y010078/1, and the project “Integrated Heating and Cooling Networks with Heat-Sharing-Enabled Smart Prosumers”, Grant EP/T022795/1.

Data availability

Data will be made available on request.

Appendix A. Mathematical models of main 5GDHC network components

This appendix summarises the mathematical models used for the main auxiliary components of the 5GDHC network, namely the buffer tank, heat exchanger, and hydraulic pump. These component models are not developed here in detail, as they are adopted from [39]. For completeness, only the main governing equations and assumptions are presented, while the reader is referred to [39] for further derivation and implementation details.

The buffer tank is modelled as a fully mixed volume; therefore, its temperature is assumed to be uniform at each time step. A finite-difference energy balance is used to update the tank temperature from time t to $t + \Delta t$:

$$T^{bt}_{t+\Delta t} = T^{bt}_{t} + \frac{\left(Q^{hp} - Q^{bt}_{o} + U^{bt} A^{bt}\left(T^{amb} - T^{bt}_{t}\right)\right)\Delta t}{c_p m^{bt}}, \tag{A.1}$$

where T^{bt}_{t} is the tank temperature at the start of the time step, Q^{hp} is the heat-transfer rate from the heat pump to the tank, which is negative in cooling mode, Q^{bt}_{o} is the heat extracted from the tank by the load side, m^{bt} is the water mass in the tank, U^{bt} is the overall tank heat-transfer coefficient, A^{bt} is the tank surface area, and T^{amb} is the ambient temperature surrounding the tank.

The heat exchanger is modelled as a counter-flow unit using the effectiveness–NTU method. The heat-exchanger effectiveness is defined as

$$\varepsilon = \frac{Q^{hx}}{c^{hx}_{\min}\left(T^{hx}_{h,i} - T^{hx}_{c,i}\right)}, \tag{A.2}$$

where Q^{hx} is the heat-transfer rate, $c^{hx}_{\min}$ is the minimum heat-capacity rate between the hot and cold streams, and $T^{hx}_{h,i}$ and $T^{hx}_{c,i}$ are the inlet temperatures of the hot and cold streams, respectively.

For a counter-flow heat exchanger, the effectiveness is given by

$$\varepsilon = \begin{cases} \dfrac{1 - \exp\left[-NTU(1-r)\right]}{1 - r\exp\left[-NTU(1-r)\right]}, & r < 1, \\ \dfrac{NTU}{1 + NTU}, & r = 1, \end{cases} \tag{A.3}$$

with

$$r = \frac{c^{hx}_{\min}}{c^{hx}_{\max}}, \tag{A.4}$$

and

$$NTU = \frac{U^{hx} A^{hx}}{c^{hx}_{\min}}, \tag{A.5}$$

where $U^{hx}A^{hx}$ is the overall heat-transfer conductance.

Once Q^{hx} is obtained, the outlet temperatures of the hot and cold streams are calculated as

$$T^{hx}_{h,o} = T^{hx}_{h,i} - \frac{Q^{hx}}{c^{hx}_h}, \tag{A.6}$$

$$T^{hx}_{c,o} = T^{hx}_{c,i} + \frac{Q^{hx}}{c^{hx}_c}, \tag{A.7}$$

where c^{hx}_h and c^{hx}_c are the heat-capacity rates of the hot and cold streams, respectively.

The hydraulic pump is represented through its pressure-rise requirement and electrical power consumption. The pump power is calculated from the water mass flow rate, $\dot{m}$, the pressure increase across the pump, Δp, the water density, ρ, and the overall pump efficiency, η:

$$P = \frac{\dot{m}\Delta p}{\rho\eta}. \tag{A.8}$$

This formulation gives the electrical power required to deliver the prescribed mass flow rate through the hydraulic circuit. The models presented above are sufficient for the integrated annual simulations carried out in this work.

Appendix B. Stratification effect on the accuracy results

Although the composite borehole model was previously validated in [29], a sensitivity analysis of the number of nodes was carried out here to justify the reduced discretisation adopted in the main study, particularly in the thickest soil layer, Layer 3, which is 170 m deep. In the finite line-source (FLS) formulation, increasing the number of nodes also increases the size of the algebraic system solved at each time step. For the eight-borehole field considered here, the baseline six-node model requires approximately 287 equations and around 180 min of computing time for one year of simulation in TRNSYS on a computer with a 13th Gen Intel Core i5-1335U processor at 1.30 GHz and 16 GB RAM. By contrast, refining Layer 3 to 20 nodes, giving 24 nodes in total (Fig. B.29), increases the system size to approximately 1295 equations and the simulation time to about 48 h. This comparison highlights the need to balance thermal resolution against computational cost.

Figs. B.30 and B.31 compare the soil-node temperatures predicted by the six-node model, denoted by subscript A, and the 24-node model, denoted by subscript B. In Layers 1 and 2, the effect of refinement is limited. The maximum deviations are about 0.5 °C in Layer 1 and 0.62 °C in Layer 2. The refined discretisation produces a slightly smoother thermal response.

The largest differences appear in Layer 3 (Fig. B.31), where the refined discretisation resolves the vertical temperature evolution more clearly during summer charging. In particular, the 24-node model captures a change in the ordering of node temperatures with depth, as mid-

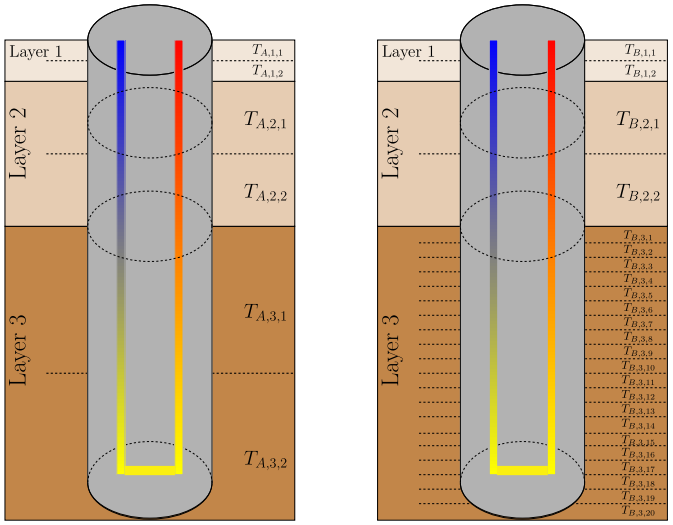


Fig. B.29. Axial discretisation schemes used to assess the effect of stratification: baseline six-node model and refined 24-node model.

layer nodes warm more rapidly than deeper nodes during the charging period. This behaviour is less evident in the six-node model because the coarser discretisation smooths the axial temperature gradient. However, the overall seasonal trend remains similar in both models.

Despite these node-level differences, the impact on the main system-level outputs is small. Fig. B.32 compares the borehole-field inlet and outlet temperatures predicted by both models. Because the heat-pump on/off controller responds to supply temperatures, differences between the two discretisations are most apparent during summer operation and seasonal transitions. To quantify these differences, filtered inlet and outlet temperature signals were compared for the six-node model, A', and the 24-node model, B'. The maximum inlet-temperature error is about 1.5 °C, occurring mainly during the transition from heating to cooling, with a mean squared error of 0.28. For the outlet temperature, the maximum error is about 0.8 °C, with a mean squared error of 0.27.

Overall, the baseline six-node discretisation is adequate for the system-level analysis carried out in this work. Although the refined 24-node model provides greater detail in representing axial temperature gradients, especially in the thickest layer during summer charging, its influence on borehole inlet and outlet temperatures is limited relative to the substantial increase in computational cost. Therefore, the reduced discretisation offers an appropriate compromise between numerical resolution and simulation efficiency for annual integrated-system studies.

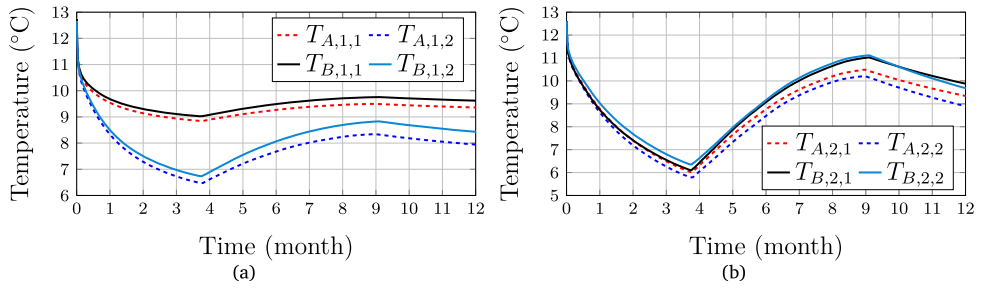


Fig. B.30. Comparison of soil-node temperatures between the six-node and 24-node borehole models for: (a) Layer 1 and (b) Layer 2.

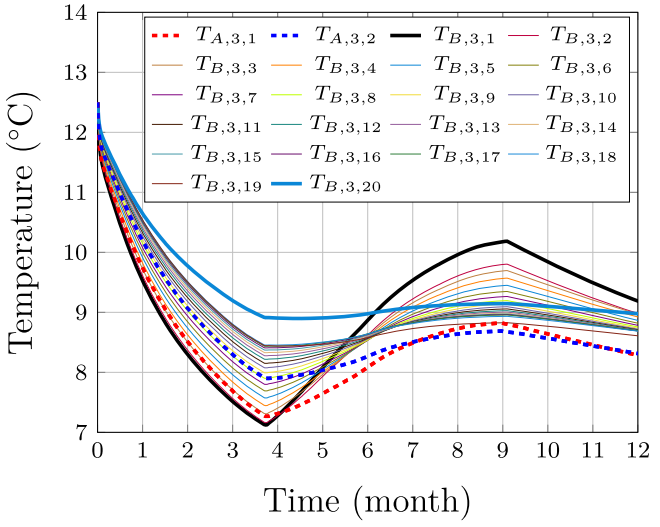


Fig. B.31. Temperature of the nodes in layer 3 of the 6 and 24 nodes borehole models.

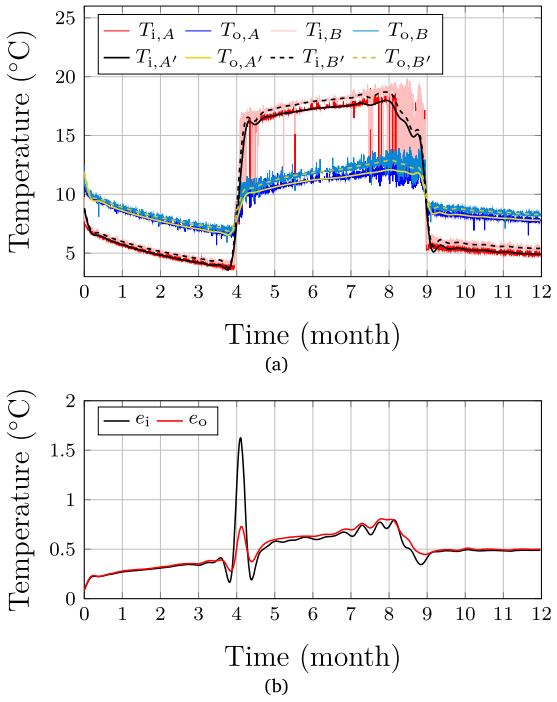


Fig. B.32. Comparison between the six-node and 24-node borehole models for borehole-field inlet and outlet temperatures: (a) filtered temperature signals; (b) resulting error between both discretisations.

Appendix C. Heat-pump model and performance curves

Each building was connected to the 5GDHC network through a decentralised single-stage water-to-water heat pump represented using TRNSYS Type 927. The heat pump employed in the analysis has a rated heating capacity of (6 kW) and nominal source- and load-side mass flow rates of (0.33 kg/s). The source side is connected to the ambient network and borehole field, whereas the load side supplies heating or cooling to the building-side buffer tank.

Separate heating and cooling performance maps define the load-side thermal capacity and electrical power consumption as functions of the source-side entering-fluid temperature, load-side entering-fluid temperature, source-side mass flow rate, and load-side mass flow rate. At each simulation time step, Type 927 interpolates within the corresponding performance map using the instantaneous operating conditions. The heating and cooling coefficients of performance are calculated as ($COP_H = Q_H/P_H$) and ($COP_C = Q_C/P_C$), where (Q_H) and (Q_C) are the useful heating and cooling capacities, respectively, and (P_H) and (P_C) are the corresponding electrical power inputs. Consequently, the model does not assume a constant COP; instead, the heat-pump capacity, electrical consumption, and COP vary with the source- and load-side operating conditions.

Fig. C.33(a) presents the heating performance map of the water-to-water heat pump used in this study. The map comprises four curves corresponding to constant load-side entering-fluid temperatures of 35°C, 40°C, 45°C, and 50°C. The source-side entering-fluid temperature range from 5°C to 10°C, which represents the operating region relevant to the annual simulations, is highlighted by dashed lines. Within this region, the COP values relevant to the simulated operating conditions range from approximately 3.95 to 4.70 for the 40°C curve. For a given load-side temperature, the COP increases as the source-side temperature rises because the required temperature lift is reduced. Conversely, at a given source-side temperature, the COP decreases as the load-side temperature increases.

Fig. C.33(b) shows the influence of the source- and load-side mass flow rates at source-side entering-fluid temperatures of 6°C, 8°C, and 10°C, and a load-side entering-fluid temperature of 39°C. The subscripts *a*, *b*, and *c* denote constant load-side mass flow rates of 0.10 kg/s, 0.20 kg/s, and 0.33 kg/s, respectively, while the source-side mass flow rate varies from 0.10 kg/s to 0.33 kg/s. Because both inlet temperatures remain constant within each set of curves, the observed COP increase is attributable to the higher mass flow rates. Overall, the hydraulic conditions produce a COP variation of approximately 0.7–0.8 units.

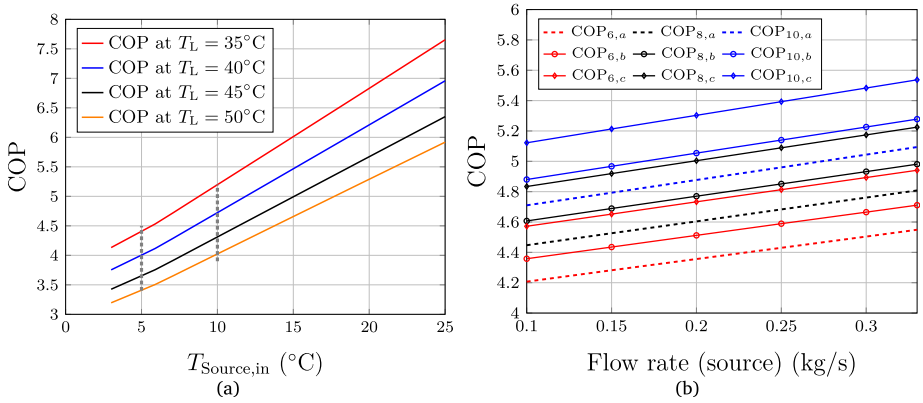


Fig. C.33. Heating-mode COP performance: (a) temperature performance map and (b) mass-flow-rate performance curves.

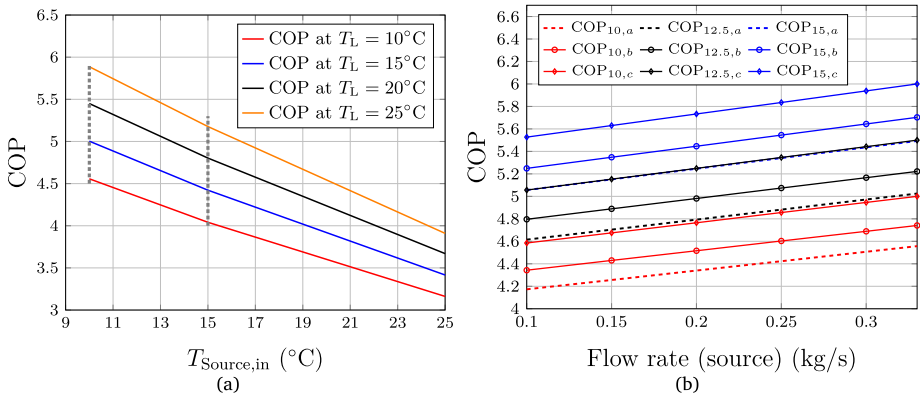


Fig. C.34. Cooling-mode COP performance: (a) temperature performance map and (b) mass-flow-rate performance curves.

Fig. C.34(a) presents the cooling COP curves for constant load-side entering-fluid temperatures of 10°C, 15°C, 20°C, and 25°C, while the source-side entering-fluid temperature varies from 10°C to 25°C. This source-temperature range covers the borehole-field outlet temperatures encountered during summer operation. At a load-side temperature of 20°C, the COP decreases from 5.45 to 4.80 as the source-side temperature increases from 10°C to 15°C, because heat rejection becomes less favourable and the temperature lift increases.

Fig. C.34(b) shows the influence of the mass flow rates at a constant load-side entering-fluid temperature of 20°C and source-side temperatures of 10°C, 12.5°C, and 15°C. The subscripts *a*, *b*, and *c* denote constant load-side mass flow rates of 0.10kg/s, 0.20kg/s, and 0.33kg/s, respectively, while the source-side mass flow rate varies from 0.10kg/s to 0.33kg/s. Because both inlet temperatures remain constant within each set of curves, the observed COP variation is attributable to the mass flow rates. The COP increases with the source-side mass flow rate, while higher load-side mass flow rates shift the curves towards higher COP values. Overall, the hydraulic conditions produce a COP variation of approximately 0.8–0.9 units.

Appendix D. Effect of inter-borehole spacing

To assess the influence of the compact 4 m spacing adopted in the main analysis, additional simulations were performed for inter-borehole distances of 5, 6, and 8 m using the Option 4 field arrangement defined in Appendix E. All cases were simulated under identical operating conditions using configuration υ, without groundwater influence, as this represents the most thermally challenging ground condition considered in the study. Since the objective of this work is the integration of the borehole field with the 5GDHC system rather than optimisation of borehole spacing, the comparison was limited to the most relevant ground-side variables: borehole-field inlet and outlet temperatures and soil-layer temperatures. A broader sensitivity analysis including network- and building-side variables would require a substantially larger parametric study and is therefore beyond the scope of the present work.

Fig. D.35 compares the borehole-field outlet and inlet temperatures for spacings of 4, 5, 6, and 8 m. The subscripts 4m, 5m, 6m, and 8m denote the corresponding inter-borehole distances. As expected, increasing the spacing reduces thermal interference and results in higher borehole outlet temperatures. The differences are more noticeable during the initial thermal transient; however, as the ground approaches a more stable seasonal response, the differences relative to the 4 m case become comparatively small. By the end of the second heating season, the outlet temperature is approximately 0.2 °C higher for 5 m spacing, 0.5 °C higher for 6 m, and 0.8 °C higher for 8 m.

Fig. D.36 shows the corresponding temperature evolution of the six soil nodes. Increasing the borehole spacing reduces the thermal interaction between neighbouring boreholes, with the 8 m case showing the smallest temperature disturbance. Nevertheless, after the initial transient, the soil temperatures also progressively approach a more stable seasonal behaviour, and the difference at the deepest node, N_6, remains approximately 1 °C between the 4 and 8 m cases. Although larger spacing improves thermal performance, urban borehole installations may be constrained by available ground area. The results therefore indicate that the adopted 4 m spacing provides acceptable thermal conditions under the restrictive conditions considered, supporting its use as a compact case-study configuration rather than as a generally optimal borehole spacing.

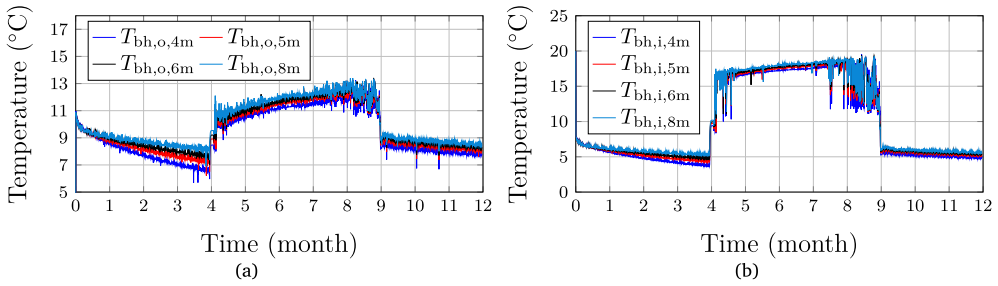


Fig. D.35. Effect of inter-borehole spacing on borehole-field temperatures: (a) outlet temperature and (b) inlet temperature for spacings of 4, 5, 6, and 8 m.

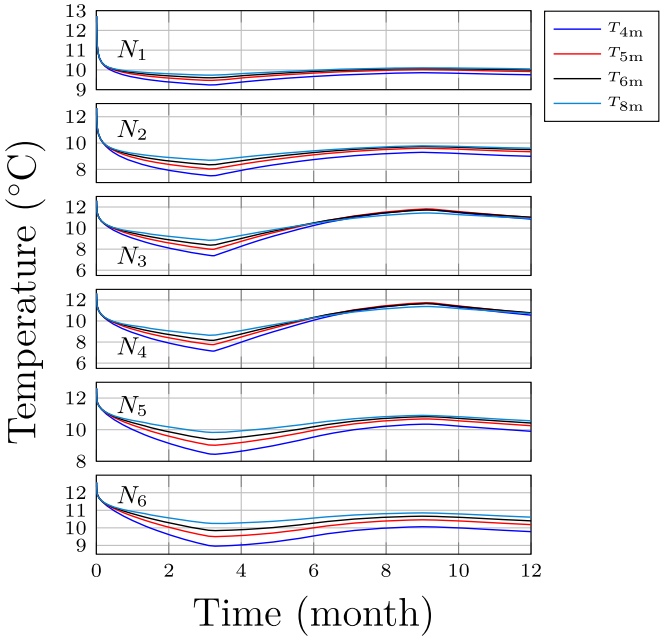


Fig. D.36. Effect of inter-borehole spacing on the temperature evolution of the six soil-layer nodes for spacings of 4, 5, 6, and 8 m.

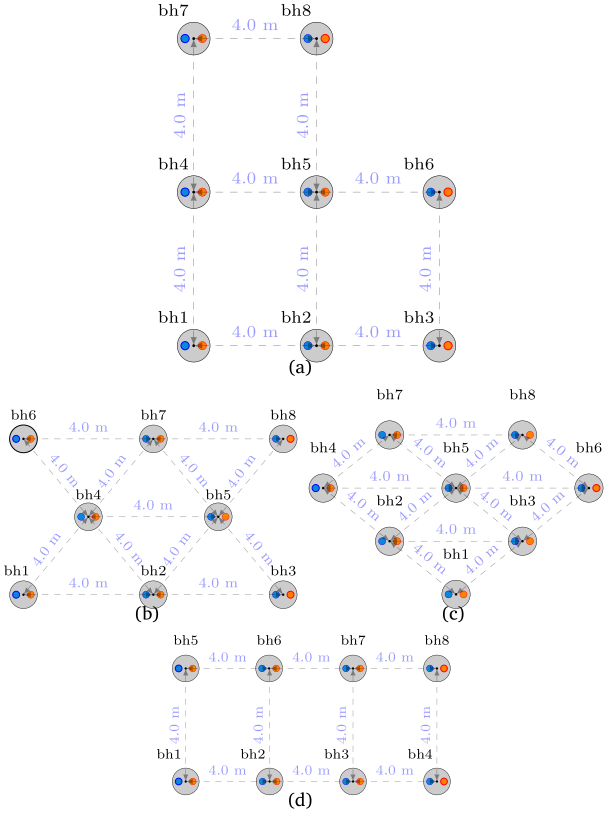


Fig. E.37. Alternative eight-borehole field configurations evaluated: (a) Option 2, (b) Option 3, (c) Option 4 and (d) Option 5.

Appendix E. Borehole field configuration

A borehole spacing of 4 m was adopted in the present case study as a compact configuration intended to represent the spatial constraints that may arise in urban 5GDHC implementations. This value is not intended to represent a generally applicable or optimal borehole spacing; rather, it provides a restrictive configuration for assessing whether acceptable thermal performance can be maintained when the available ground area is limited. The influence of this assumption is further assessed through additional simulations with borehole spacings of 5, 6, and 8 m. For completeness, five eight-borehole field arrangements were also assessed in the present work, including the layout selected for the main analysis: Option 1, with one central borehole surrounded by seven peripheral boreholes.

To isolate the influence of borehole-field geometry from the additional assumptions associated with the simplified groundwater representation, the layout comparison was conducted using the no-groundwater configuration, configuration *v*. The comparison therefore represents conduction-dominated conditions only and does not account for direction-dependent thermal-plume transport or upstream-downstream interference caused by groundwater advection. The four alternative layouts are shown in Fig. E.37: a near-matrix arrangement (Option 2), a triangular arrangement (Option 3), a diamond-shaped arrangement (Option 4), and two rows of four boreholes (Option 5). All configurations were simulated over one year under identical operating conditions.

Since each arrangement contains eight boreholes and each borehole is discretised into six axial nodes, a complete node-by-node comparison would be unnecessarily extensive. Instead, three global indicators were used to compare the layouts: (i) the minimum soil-node temperature, (ii) the maximum soil-node temperature, and (iii) the borehole outlet temperature. For indicators (i) and (ii), the extreme values may occur in different boreholes within the same configuration.

Figs. E.38 and E.39 present the minimum and maximum soil-node temperatures for each layout, where the subscript optX identifies the corresponding option. The results show only slight differences between configurations, indicating that the field arrangement has a relatively limited influence under the conditions analysed. Among the five options, Option 4 exhibits the strongest spatial non-uniformity, with both the lowest minimum temperatures and the highest maximum temperatures across the field. Option 5 gives the warmest minimum temperatures, whereas Option 1 gives the lowest maximum temperatures. The range of maximum soil-node temperatures is small, approximately 0.12–0.37 °C, while the difference in minimum temperature is larger, around 0.33–0.8 °C. Overall, these results suggest that layout mainly

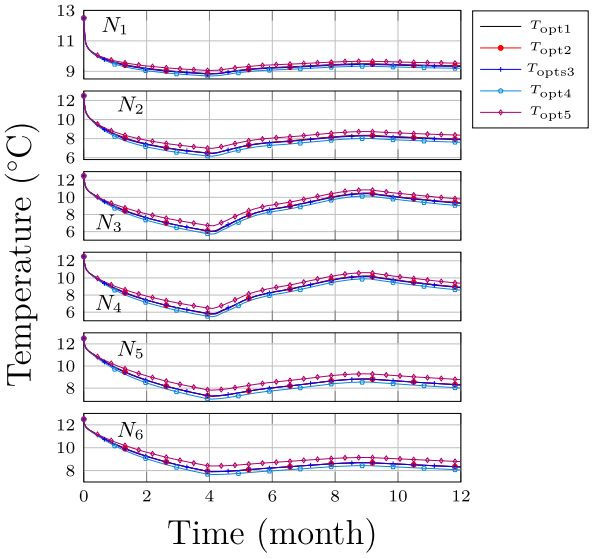


Fig. E.38. Minimum soil-node temperatures over the annual simulation for the five borehole-field configurations.

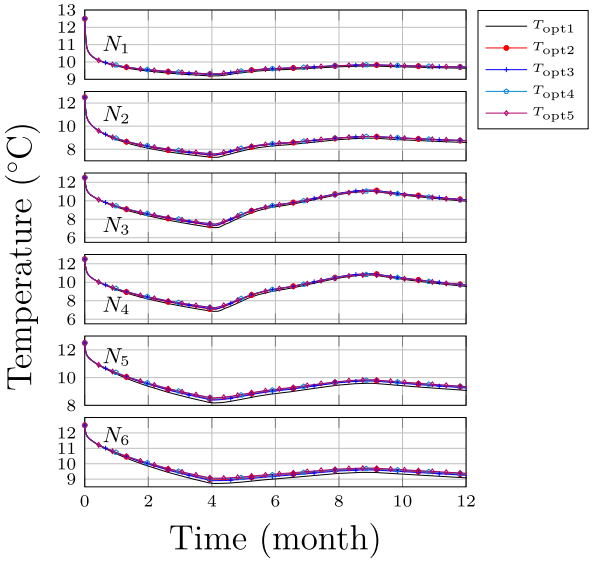


Fig. E.39. Maximum soil-node temperatures over the annual simulation for the five borehole-field configurations.

affects the uniformity of the thermal field rather than producing major differences in average thermal performance.

The comparison of borehole-field outlet temperatures in Fig. E.40 leads to the same conclusion. In heating mode, where a higher outlet temperature is desirable, the sensitivity to layout is limited: the difference between the best case, Option 5, and the least favourable case, Option 4, is only about 0.25 °C. Under the heat-pump performance assumed in this study, such a difference is too small to produce a meaningful change in COP and is therefore secondary compared with other uncertainties, such as soil properties or seasonal load imbalance. In cooling mode, the relative ranking is partially reversed, with Option 4 giving the warmest outlet temperature and therefore the least favourable cooling performance.

Given these small differences, Option 1 was selected for the main analysis because it provides intermediate behaviour between the most and least favourable cases, while also promoting a relatively uniform thermal response across the field. Therefore, under the operating conditions considered in this work, the overall conclusions are negligibly sensitive to the eight-borehole arrangement. Therefore, under the conduction-dominated conditions represented by configuration v, and for the borehole spacing and operating conditions considered in this study, the system-level results show limited sensitivity to the five investigated eight-borehole arrangements. This conclusion should not be extrapolated to sites with significant directional groundwater advection. Option 1 was consequently selected as a representative and thermally balanced arrangement for the subsequent system-level simulations, rather than as a groundwater-specific optimum.

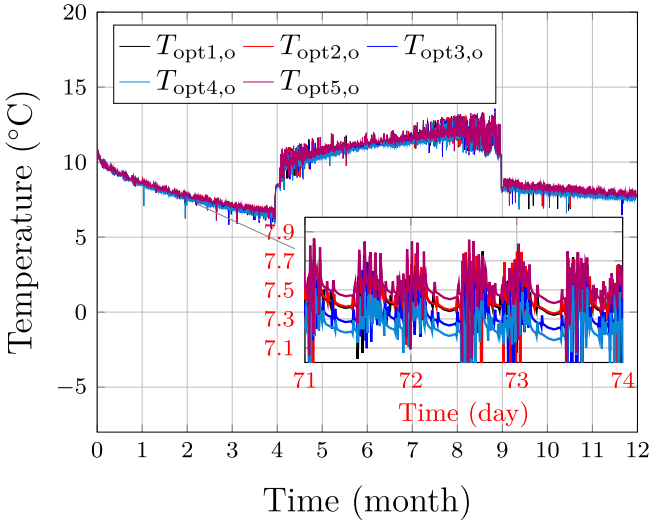


Fig. E.40. Borehole outlet temperature over the annual simulation for the five borehole-field configurations.

References

[1] United Nations Environment Programme, Global Status Report for Buildings and Construction 2024/2025, Technical Report, United Nations Environment Programme, Paris, France, 2025. https://www.unep.org/resources/report/global-status-report-buildings-and-construction-20242025. https://doi.org/10.59117/20.500.11822/47214

[2] International Energy Agency, Energy Efficiency 2025, Technical Report, International Energy Agency, Paris, France, 2025. https://www.iea.org/reports/energy-efficiency-2025.

[3] H. Sadeghi, A. Ijaz, R.M. Singh, Current status of heat pumps in Norway and analysis of their performance and payback time, Sustain. Energy Technol. Assess. 54 (2022) 102829. https://doi.org/10.1016/j.seta.2022.102829

[4] X. Li, S. Yilmaz, M.K. Patel, J. Chambers, et al., Techno-economic analysis of fifth-generation district heating and cooling combined with seasonal borehole thermal energy storage, Energy 285 (2023) 129382. https://doi.org/10.1016/j.energy.2023.129382

[5] K. Kontu, S. Rinne, S. Junnila, et al., Introducing modern heat pumps to existing district heating systems – global lessons from viable decarbonizing of district heating in Finland, Energy 166 (2019) 862–870. https://doi.org/10.1016/j.energy.2018.10.077

[6] S. Yao, J. Wu, M. Qadrdan, A state-of-the-art analysis and perspectives on the 4th/5th generation district heating and cooling systems, Renew. Sustain. Energy Rev. 202 (2024) 114729. https://doi.org/10.1016/j.rser.2024.114729

[7] K. Gjoka, B. Rismanchi, R.H. Crawford, Fifth-generation district heating and cooling systems: a review of recent advancements and implementation barriers, Renew. Sustain. Energy Rev. 171 (2023) 112997. https://doi.org/10.1016/j.rser.2022.112997

[8] S. Buffa, M. Cozzini, M. D'Antoni, M. Baratieri, R. Fedrizzi, 5th generation district heating and cooling systems: a review of existing cases in Europe, Renew. Sustain. Energy Rev. 104 (2019) 504–522. https://doi.org/10.1016/j.rser.2018.12.059

[9] S. Boesten, W. Ivens, S.C. Dekker, H. Eijdems, 5th generation district heating and cooling systems as a solution for renewable urban thermal energy supply, in: Advances in Geosciences, Vol. 49, Copernicus GmbH, 2019, pp. 129–136. ISSN: 1680-7340. https://doi.org/10.5194/adgeo-49-129-2019

[10] K. Gjoka, B. Rismanchi, R.H. Crawford, Fifth-generation district heating and cooling: opportunities and implementation challenges in a mild climate, Energy 286 (2024) 129525. https://doi.org/10.1016/j.energy.2023.129525

[11] M. Wirtz, T. Schreiber, D. Müller, Survey of 53 fifth-generation district heating and cooling (5GDHC) networks in Germany, Energy Technol. 10 (11) (2022) 2200749. https://doi.org/10.1002/ente.202200749

[12] R. Zeh, B. Ohlsen, D. Philipp, D. Bertermann, T. Kotz, N. Jocić, V. Stockinger, Large-scale geothermal collector systems for 5th generation district heating and cooling

networks, Sustainability 13 (11) (2021) 6035. Publisher: Multidisciplinary Digital Publishing Institute. https://doi.org/10.3390/su13116035
[13] J.S. Figueira, A. García Gil, A. Vieira, A.K. Michopoulos, D.P. Boon, F. Loveridge, F. Cecinato, G. Götzl, J. Epting, K. Zosseder, M. Bloemendal, M. Woods, P. Christodoulides, P.J. Vardon, S.P. Borg, S. Erbs Poulsen, T.R. Andersen, Shallow geothermal energy systems for district heating and cooling networks: review and technological progression through case studies, Renew. Energy 236 (2024) 121436. https://doi.org/10.1016/j.renene.2024.121436
[14] H. Sadeghi, R. Jalali, R.M. Singh, A review of borehole thermal energy storage and its integration into district heating systems, Renew. Sustain. Energy Rev. 192 (2024) 114236. https://doi.org/10.1016/j.rser.2023.114236
[15] M. Lanahan, P.C. Tabares-Velasco, Seasonal thermal-energy storage: a critical review on BTES systems, modeling, and system design for higher system efficiency, Energies 10 (6) (2017) 743. Publisher: Multidisciplinary Digital Publishing Institute. https://doi.org/10.3390/en10060743
[16] B. Sibbitt, D. McClenahan, R. Djebbar, J. Thornton, B. Wong, J. Carriere, J. Kokko, The performance of a high solar fraction seasonal storage district heating system – five years of operation, Energy Procedia 30 (2012) 856–865. https://doi.org/10.1016/j.egypro.2012.11.097
[17] L. Mesquita, D. McClenahan, J. Thornton, J. Carriere, B. Wong, Drake landing solar community: 10 years of operation, in: Proceedings of SWC2017/SHC2017, International Solar Energy Society, Abu Dhabi, 2017, pp. 1–12. https://doi.org/10.18086/swc.2017.06.09
[18] L.M. Dang, L.Q. Nguyen, J. Nam, T.N. Nguyen, S. Lee, H.-K. Song, H. Moon, Fifth generation district heating and cooling: a comprehensive survey, Energy Rep. 11 (2024) 1723–1741. https://doi.org/10.1016/j.egyr.2024.01.037
[19] C. Zhi, X. Zhou, X. Hong, A. Wang, W. Ye, X. Zhang, H. Chen, Field study of the long-term performance and reliability of large-scale ground source heat pump systems applied to a mixed-use complex of buildings, Renew. Energy 241 (2025) 122344. https://doi.org/10.1016/j.renene.2025.122344
[20] S. Kavanaugh, K. Rafferty, Geothermal Heating and Cooling: Design of Ground-Source Heat Pump Systems, ASHRAE, 2014.
[21] M. Ahmadfard, M. Bernier, Sizing vertical ground heat exchangers, ASHRAE J. 63 (12) (2021) 24–36.
[22] W. Gao, M. Qadrdan, M. Chaudry, J. Wu, Seasonal storage of heat in boreholes, Technical Note, UK Energy Research Centre (UKERC) (2023).
[23] A.V. Miceli, A. Buscemi, S. Guarino, M. Beccali, V. Lo Brano, Modelling of borehole thermal energy storages: a g-function approach with a novel load aggregation scheme, Energy Convers. Manag. 348 (2026) 120666. https://doi.org/10.1016/j.enconman.2025.120666
[24] L. Lamarche, B. Beauchamp, A new contribution to the finite line-source model for geothermal boreholes, Energy Build. 39 (2) (2007) 188–198. https://doi.org/10.1016/j.enbuild.2006.06.003
[25] M. Cimmino, M. Bernier, A semi-analytical method to generate *g*-functions for geothermal bore fields, Int. J. Heat Mass Transf. 70 (2014) 641–650. https://doi.org/10.1016/j.ijheatmasstransfer.2013.11.037
[26] M. Cimmino, Fast calculation of the *g* -functions of geothermal borehole fields using similarities in the evaluation of the finite line source solution, J. Build. Perform. Simul. 11 (6) (2018) 655–668. https://doi.org/10.1080/19401493.2017.1423390
[27] S. Erol, B. François, Multilayer analytical model for vertical ground heat exchanger with groundwater flow, Geothermics 71 (2018) 294–305. https://doi.org/10.1016/j.geothermics.2017.09.008
[28] J. Hu, An improved analytical model for vertical borehole ground heat exchanger with multiple-layer substrates and groundwater flow, Appl. Energy 202 (2017) 537–549. https://doi.org/10.1016/j.apenergy.2017.05.152
[29] W. Gao, M. Qadrdan, A composite analytical model to predict the thermal performance of borehole ground heat exchangers within stratified ground, Appl. Therm. Eng. 258 (2025) 124668. https://doi.org/10.1016/j.applthermaleng.2024.124668
[30] A.M. Chaudhry, J. Hachez, S. Chicherin, G. Ghorbaniasl, S. Bram, Potential site evaluation of fifth-generation district heating and cooling networks under uncertain energy market conditions: a two-step robust design analysis approach, Energy 311 (2024) 133334. https://doi.org/10.1016/j.energy.2024.133334
[31] D. Romanov, I. Chakraborty, S. Holler, Comparative analysis of scenarios of data center waste heat utilization for district heating networks of different generations, Energy Convers. Manag. 334 (2025) 119856. https://doi.org/10.1016/j.enconman.2025.119856
[32] X. Li, S. Yilmaz, M.K. Patel, J. Chambers, Techno-economic analysis of fifth-generation district heating and cooling combined with seasonal borehole thermal energy storage, Energy 285 (2023) 129382. https://doi.org/10.1016/j.energy.2023.129382
[33] M. Fiorentini, P. Heer, L. Baldini, Design optimization of a district heating and cooling system with a borehole seasonal thermal energy storage, Energy 262 (2023) 125464. https://doi.org/10.1016/j.energy.2022.125464
[34] A. Pour Ahmadiyan, N. Nord, Seasonal storage of district heating surplus heat through borehole thermal energy storage: a global sensitivity analysis, Renew. Energy 261 (2026) 125300. https://doi.org/10.1016/j.renene.2026.125300
[35] J. Yang, K. Soga, M. Sulzer, K. Chen, Optimizing district energy systems by integrating borehole thermal energy storage using a mixed-integer linear programming *g*-function framework with a multi-timescale rolling horizon method, Energy 354 (2026) 141111. https://doi.org/10.1016/j.energy.2026.141111
[36] K. Droste, A. Schwartz, Implementation of a machine learning supported model predictive control for a 5th generation district heating and cooling energy hub, Energy AI 24 (2026) 100699. https://doi.org/10.1016/j.egyai.2026.100699
[37] H. Averfalk, T. Benakopoulos, I. Best, F. Dammel, C. Engel, R. Geyer, O. Gudmundsson, K. Lygnerud, N. Nord, J. Oltmanns, K. Ponweiser, D. Schmidt, H. Schrammel, D.S. Østergaard, S. Svendsen, M. Tunzi, S. Werner, Low-Temperature District Heating Implementation Guidebook: Final Report of IEA DHC Annex TS2 Implementation of Low-Temperature District Heating Systems, Fraunhofer-Verlag, 2021.
[38] M. Taylor, M. Qadrdan, B. Woodman, J. Wu, The future of district heating and cooling networks, Working Paper, UK Energy Research Centre (UKERC), (2023).
[39] M. Taylor, W. Gao, S. Masum, M. Qadrdan, Techno-economic assessment of bi-directional low temperature networks, Appl. Energy 347 (2023) 121202. https://doi.org/10.1016/j.apenergy.2023.121202
[40] J. Lindhe, S. Javed, D. Johansson, H. Bagge, A review of the current status and development of 5GDHC and characterization of a novel shared energy system, Sci. Technol. Built Environ. 28 (5) (2022) 595–609. https://doi.org/10.1080/23744731.2022.2057111
[41] D. Bauer, W. Heidemann, H. Müller-Steinhagen, H.J.G. Diersch, Thermal resistance and capacity models for borehole heat exchangers, Int. J. Energy Res. 35 (4) (2011) 312–320. https://doi.org/10.1002/er.1689
[42] F. Lei, P. Hu, N. Zhu, T. Wu, Periodic heat flux composite model for borehole heat exchanger and its application, Appl. Energy 151 (2015) 132–142. https://doi.org/10.1016/j.apenergy.2015.04.035
[43] S.J. Rees, Advances in Ground-Source Heat Pump Systems, Woodhead Publishing, 2016. ISBN: 9780081003114.
[44] X. Liu, J. Wu, N. Jenkins, A. Bagdanavicius, Combined analysis of electricity and heat networks, Appl. Energy 162 (2016) 1238–1250. https://doi.org/10.1016/j.apenergy.2015.01.102
[45] M. Pirouti, Modelling and Analysis of a District Heating Network, Ph.D. thesis, School of Engineering, Cardiff University, Cardiff, UK, 2013. Accessed: 12 August 2026, https://orca.cardiff.ac.uk/id/eprint/45201/1/Marouf.Pirouti_PhD%20Thesis.pdf.
[46] F. Chen, J. Mao, S. Chen, C. Li, P. Hou, L. Liao, Efficiency analysis of utilizing phase change materials as grout for a vertical U-tube heat exchanger coupled ground source heat pump system, Appl. Therm. Eng. 130 (2018) 698–709. https://doi.org/10.1016/j.applthermaleng.2017.11.062
[47] W. Li, X. Li, R. Du, Y. Wang, J. Tu, Experimental investigations of the heat load effect on heat transfer of ground heat exchangers in a layered subsurface, Geothermics 77 (2019) 75–82. https://doi.org/10.1016/j.geothermics.2018.08.011
[48] Kensa, What are ground source heat pump boreholes?, 2026, (https://kensa.co.uk/ground-source-heat-pumps/boreholes). Accessed: 2 Jan. 2026.
[49] J. Wołoszyn, Global sensitivity analysis of borehole thermal energy storage efficiency for seventeen material, design and operating parameters, Renew. Energy 157 (2020) 545–559. https://doi.org/10.1016/j.renene.2020.05.047
[50] A. Albers, P. Huttenloch, R. Zorn, H. Steger, P. Blum, Determination of thermal properties of grouting materials for borehole heat exchangers (BHE), Geotherm. Energy 12 (2024) 36. https://doi.org/10.1186/s40517-024-00316-3
[51] D.P. Boon, G.J. Farr, C. Abesser, A.M. Patton, D.R. James, D.I. Schofield, D.G. Tucker, Groundwater heat pump feasibility in shallow urban aquifers: experience from Cardiff, UK, Sci. Total Environ. 697 (2019) 133847. https://doi.org/10.1016/j.scitotenv.2019.133847
[52] Ove Arup & Partners Ltd., Barry Waterfront Environmental Statement: Chapter H—Water Resources, Drainage and Flooding, Technical Report 30327/680542v1, Ove Arup & Partners Ltd., Cardiff, UK, 2009. Available from Vale of Glamorgan Council. Accessed: 14 August 2026.
[53] C. Hanmer, M. Shipworth, D. Shipworth, E. Carter, How household thermal routines shape UK home heating demand patterns, Energy Effic. 12 (1) (2019) 5–17. https://doi.org/10.1007/s12053-018-9632-x
[54] M. Pullinger, E. Zapata-Webborn, J. Kilgour, S. Elam, J. Few, N. Goddard, C. Hanmer, E. McKenna, T. Oreszczyn, L. Webb, Capturing variation in daily energy demand profiles over time with cluster analysis in British homes (September 2019 – August 2022), Appl. Energy 360 (2024) 122683. https://doi.org/10.1016/j.apenergy.2024.122683
[55] Department for Energy and Zero, Raising product standards for space heating: updating ecodesign and energy labelling for hydronic space and combination heaters, 2024. Accessed: 14 August 2026, https://www.gov.uk/government/consultations/raising-product-standards-for-space-heating/raising-product-standards-for-space-heating-updating-ecodesign-and-energy-labelling-for-hydronic-space-and-combination-heaters-html.
[56] L. Corcoran, P. Saikia, C.E. Ugalde-Loo, M. Abeysekera, Thermal energy demand database for typical British dwellings, Appl. Energy 411 (2026) 127573. https://doi.org/10.1016/j.apenergy.2026.127573
[57] C. Parsloe, Design Guide: Heat Networks, Chartered Institution of Building Services Engineers (CIBSE), London, UK, 2021.
[58] G. Emmi, A. Zarrella, M. De Carli, S. Moretto, A. Galgaro, M. Cultrera, M. Di Tuccio, A. Bernardi, Ground source heat pump systems in historical buildings: two Italian case studies, Energy Procedia 133 (2017) 183–194. https://doi.org/10.1016/j.egypro.2017.09.383
[59] G. Emmi, M. Bottarelli, Energy performance of ground source heat pump systems with flat-panel ground heat exchangers, Energy Effic. 18 (7) (2025) 73. https://doi.org/10.1007/s12053-025-10344-y
[60] M. Bilardo, F. Sandrone, G. Zanzottera, E. Fabrizio, Modelling a fifth-generation bidirectional low temperature district heating and cooling (5GDHC) network for nearly zero energy district (nZED), Energy Rep. 7 (2021) 8390–8405. https://doi.org/10.1016/j.egyr.2021.04.054
[61] G. Viviescas, M. Bernier, A water-to-water heat pump model with experimental validation, Energies 17 (8) (2024) 1858. https://doi.org/10.3390/en17081858
[62] T. Ohtani, K. Soma, I. Masaki, Development of resource map for open-loop ground source heat pump system based on heating and cooling experiments, Appl. Sci. 15 (16) (2025) 9195. https://doi.org/10.3390/app15169195